Seismic tomography of Nabro caldera, Eritrea: insights into the magmatic and hydrothermal systems of a recently erupted volcano

Miriam Gauntlett[1], Thomas Samuel Hudson[1], John-Michael Kendall[1], Nicholas Rawlinson[2], Jon D Blundy[3], Sacha Lapins[4], Berhe Goitom[4], James Oliver Scott Hammond[5], Clive Oppenheimer[2], and Ghebrebrhan Ogubazghi[6]

[1]University of Oxford
[2]University of Cambridge
[3]Oxford University
[4]University of Bristol
[5]Birkbeck, University of London
[6]University of Asmara

October 13, 2022

Seismic tomography of Nabro caldera, Eritrea: insights into the magmatic and hydrothermal systems of a recently erupted volcano

M. Gauntlett[1], T. Hudson[1], J-M. Kendall[1], N. Rawlinson[2], J. Blundy[1], S. Lapins[3], B. Goitom[3], J. Hammond[4], C. Oppenheimer[5], G. Ogubazghi[6]

[1]Department of Earth Sciences, University of Oxford, UK
[2]Bullard Laboratories, Department of Earth Sciences, University of Cambridge, UK
[3]School of Earth Sciences, University of Bristol, UK
[4]Department of Earth and Planetary Sciences, Birkbeck, University of London, UK
[5]Department of Geography, University of Cambridge, UK
[6]Eritrea Institute of Technology, Eritrea

Key Points:

- 3D seismic modelling reveals the structure of the magmatic and hydrothermal systems beneath Nabro volcano in Eritrea.
- The primary melt storage region feeding the 2011 eruption is located at depths of 6—10 km below sea level.
- Degassing from the magma storage zone causes overpressure in partially-saturated, fractured intrusive complex above.

Corresponding author: Miriam Gauntlett, `miriam.gauntlett@linacre.ox.ac.uk`

Abstract

Understanding the crustal structure and the storage and movement of fluids beneath a volcano is necessary for characterising volcanic hazard, geothermal prospects and potential mineral resources. This study uses local earthquake traveltime tomography to image the seismic velocity structure beneath Nabro, an off-rift volcano located within the central part of the Danakil microplate near the Ethiopia-Eritrea border. Nabro underwent its first historically-documented eruption in June 2011, thereby providing an opportunity to analyse its post-eruptive state by mapping subsurface fluid distributions. We use a catalog of earthquakes detected on a temporary seismic array using machine learning methods to simultaneously relocate the seismicity and invert for the three-dimensional P- and S-wave velocity structures (V_P, V_S) and the ratio between them (V_P/V_S). Overall, our model shows higher than average P- and S-wave velocities, suggesting the presence of high-strength, solidified intrusive magmatic rocks in the crust. We identify an aseismic region of low V_P, low V_S and high V_P/V_S ratio at depths of 6–10 km b.s.l., interpreted as the primary melt storage region that fed the 2011 eruption. Above this is a zone of high V_S, low V_P and low V_P/V_S ratio, representing an intrusive complex of fractured rocks partially-saturated with over-pressurized gases. Our observations identify the persistence of magma in the subsurface following the eruption, and track the degassing of this melt through the crust to the surface. The presence of volatiles and high temperatures within the shallow crust indicate that Nabro is a viable candidate for geothermal exploration.

Plain Language Summary

Understanding the structure of the crust and the distribution and movement of fluids beneath a volcano allows for the assessment of volcanic hazard, geothermal potential and possible mineral extraction. To identify different regions of the crust and differentiate between fluids, we use the fact that the speed of seismic waves depends on the material they are travelling through. For example, seismic waves will travel through magma (molten, or liquid, rock) at lower speeds than in the surrounding rock. The focus of this study is Nabro volcano in Eritrea, which erupted in 2011. We use earthquakes that have been automatically detected following the eruption to image the structure of the crust in the form of 3D variations in seismic wave speeds. This identifies a volume of magma stored at depths of 6—10 km below sea level, which fed the eruption. Above this, we observe a region of rocks that are likely remnants of earlier eruptions at Nabro, with fractures containing gases at high pressure. The source of this high pressure is the release of gas from the magma storage zone. The presence of hot fluids means Nabro could be used as a source of geothermal power in the future.

1 Introduction

Modelling the crustal architecture of a volcano is of fundamental importance; interactions between magmatic and hydrothermal systems play a central role in volcanic unrest and eruption (e.g., Chouet & Matoza, 2013; Pritchard et al., 2019; Wilks et al., 2020). However, these systems are often poorly characterized, both due to their complexity and to the difficulty of probing the crust in sufficient detail. Further motivation for investigation is that volcanic-hosted hydrothermal systems may be a source of geothermal energy production (Reinsch et al., 2017) or metal-rich brines (Blundy et al., 2021).

Seismic body wave tomography is a powerful geophysical tool used to image the Earth's interior on various scales. It has been applied locally to deforming volcanoes in order to understand their subsurface active magmatic and hydrothermal processes (e.g., Patane et al., 2002; Chiarabba & Moretti, 2006; Korger & Schlindwein, 2014; Greenfield et al., 2016; Wilks et al., 2020; Koulakov et al., 2021). Seismic velocities of rocks are influenced by a multitude of factors, including lithology, fractures, temperature, the presence of fluids and gases, fluid saturation and porosity. Knowledge of the seismic velocity structure can therefore help to identify melt-bearing regions, hydrothermal fluids and over-pressurized gases beneath a volcano (e.g., Londoño & Sudo, 2003; Vanorio et al., 2005; Lin, 2013; Wilks et al., 2020). These observations are crucial to understanding volcanic unrest, characterising future volcanic hazard and assessing geothermal potential.

Using seismic data collected following the 2011 eruption of Nabro, we present high-resolution tomographic images of the crust with the aim of improving understanding of the post-eruptive state and dynamics at depth beneath the volcano. Nabro volcano is located on the central part of the Danakil microplate near the Ethiopia-Eritrea border in the Afar region. The Afar depression is part of the East African Rift System, an active continental rift system, and contains the triple junction between Arabian, Nubian and Somalian plates (Hammond et al., 2011). Most of the active volcanism associated with continental rifting is found along the central rift axis. However, Nabro is offset from the axis of spreading and is thus known as an "off-rift" or "off-axis" volcano (Barberi et al., 1974; Wiart & Oppenheimer, 2005). Together with the neighbouring caldera of Mallahle, Nabro makes up the Bidu Volcanic Complex. Nabro and Mallahle are characterized by large calderas, thought to have been formed circa 130 and 295 ka ago, respectively (Oppenheimer et al., 2019). The alignment of the volcanic centers bears NE-SW, striking obliquely to the NW-SE trend of the Red Sea (Wiart & Oppenheimer, 2005; Goitom et al., 2015). Nabro is the largest volcano in the Nabro Volcanic Range (NVR), which runs in a NNE-SSW direction from Bara'Ale volcano in Ethiopia to the Kod Ali formation in the Red Sea (Wiart & Oppenheimer, 2005). Nabro's summit is 2248 m above sea level, and its caldera reaches a diameter of 8 km (Wiart & Oppenheimer, 2005). It remains unclear how magma is supplied to off-rift volcanoes such as Nabro; further, their role in accommodating extension is not well understood (Maccaferri et al., 2014). Indeed, the propagation of strain transfer from the Aden and Red Sea plate boundaries into the Afar region south of Nabro is complex and transient, with active faults distributed over hundreds of thousands of square kilometres (Manighetti et al., 2001). Possible explanations for the NVR's extensive off-rift magmatism include reactivation of an older, pre-rift structure (Barberi et al., 1974) or localized diapiric upwellings from depth (Hammond et al., 2013).

On 12 June 2011, Nabro volcano underwent its first eruption on historical record—the last dated activity occurred within the caldera circa 23 ka ago (Oppenheimer et al., 2019). The volcano was unmonitored at the time of the eruption, with no geophysical surveillance networks operating in Eritrea. The eruption resulted in seven fatalities and displaced some 12,000 people (Goitom et al., 2015). The explosive activity generated significant tephra clouds and released 4.5 Tg of SO_2 into the atmosphere within the first 15 days, producing the largest stratospheric aerosol perturbation since the 1991 Pinatubo eruption (Theys et al., 2013; Fromm et al., 2014). Since the eruption, Nabro has been identified as one of the main geothermal prospects in Eritrea due to increased fumarolic activity at the surface (Yohannes, 2012).

Geodetic modelling suggests that a shallow, NW–SE-trending dyke fed the eruption, which triggered slip on parallel normal faults, consistent with the orientation of vents within the crater (Goitom et al., 2015). Petrological analysis by Donovan et al. (2018) identifies two distinct batches of magma, one more primitive and the other high in sulfur and water content. The authors propose that the latter batch underwent isobaric crystallisation in a storage region at $\sim$5–7 km depth below sea level (b.s.l.), while the more primitive batch rose rapidly to the shallow crust from depth. In the months following the eruption, Nabro experienced subsidence at a slowly decaying rate (Hamlyn et al., 2014, 2018). By inverting the deformation field, Hamlyn et al. (2018) propose a best-fitting deflating Mogi source at 6.4 ± 0.3 km depth b.s.l..

A temporary seismic network was established around Nabro in the aftermath of the eruption, operational from 31 August 2011 until October 2012. Lapins et al. (2021) trained and validated a novel deep learning model on this data in order to automatically detect phase arrivals. When deployed, the deep learning model significantly augmented the seismic catalog analysed in previous studies. From this catalog, Lapins (2021a) calculates hypocenter locations, local and moment magnitudes, path/site attenuation effects and b-values. A key result is that seismicity beneath Nabro lies above and below an inferred, aseismic magma storage zone at depths of 6–9 km b.s.l., consistent with the modelled Mogi source from previous studies (Hamlyn et al., 2014; Goitom et al., 2015) and petrological inferences about magma storage depths (Donovan et al., 2018). Events below the reservoir are thought to result from small pulses of magma or volatile migration, while events above the aseismic zone could reflect outgassing processes, migrations of fluid or melt into the reservoir or intense fracturing as a result of the observed subsidence (Lapins, 2021a). The patterns of seismicity to the northeast of Nabro indicate that deeper fluid or magmatic processes have triggered movement on a shallower fault, suggesting that fluids may play an important role in regional extensional processes (Lapins, 2021a).

Lapins (2021a) notes that one of the major limitations of their study is the lack of a well-constrained velocity model. Here, we apply seismic tomography methods to the dataset from Lapins et al. (2021) to derive a more accurate velocity model. We then use this new model to jointly carry out 3D P-wave (V_P), S-wave (V_S) and V_P/V_S tomography and earthquake hypocenter relocation, in order to yield further insight into the subsurface processes responsible for the seismicity and surface deformation at Nabro. By interpreting these tomographic images, we aim to characterize the migration and distribution of volcanic fluids in Nabro's active magmatic system. These results have particular relevance for the assessment of Nabro's geothermal energy potential, as well as its future seismic and volcanic hazard.

2 Data

2.1 Network and Data Collection

The seismic data used in the tomographic inversion were collected by a temporary local seismic network deployed in the aftermath of Nabro's 2011 eruption. Eight 3-component broadband 30 s Güralp seismometers (five CMG-6TD and three CMG-40TD) were provided by SEIS-UK to monitor Nabro's post-eruptive state (Hamlyn et al., 2014). The network was fully operational from 31 August 2011 until October 2012. However, one of the 40TD stations, NAB6, was damaged due to flooding and thus was inoperable, producing no useable data (Lapins, 2021a). NAB7 also had frequent data gaps but was still used for phase arrival picking and event location, and therefore we also use it in our tomographic inversions, along with the other six stations. The data were all initially recorded at 100 Hz sample frequency and then switched to 50 Hz sample frequency early in October 2011 (Lapins, 2021a).

Manually picking seismic phase arrivals is time-consuming, and can be especially difficult in volcanic settings due to the fact that volcano-tectonic earthquakes tend to be fairly low magnitude (< 4) events. A previous manual analysis of the Nabro seismic data only covered the time period 31 August – 31 December 2011 (Goitom, 2017), which left eight months of data unpicked. Therefore, a new deep learning model for automated phase arrival detection based on a convolutional neural network, known as U-GPD, was applied to the seismic data from the temporary network around Nabro (Lapins et al., 2021). The U-GPD model is trained and validated using 35 days of manually picked data from Goitom (2017). To overcome issues surrounding the use of a small training set, they use transfer learning on an existing deep learning model for phase arrival detection (Ross et al., 2018) trained using millions of phase arrivals from earthquakes in Southern California. The resulting U-GPD transfer learning model was shown to outperform two existing, comprehensively trained models, PhaseNet (Zhu & Beroza, 2019) and GPD (Ross et al., 2018), and the existing manual catalog in terms of pick error and number of phase arrivals detected (Lapins et al., 2021). When the automated phase arrival picks and original manual pick times are compared, the root mean square deviation for P-wave picks is 0.038 s and for S-wave picks it is 0.053 s (Figure 6 in Lapins (2021a)). The model is far more efficient than manual phase picking, processing the 14 months of seismic data in less than 4 hours. . The three output channels of the U-GPD model give the probability of a P-wave arrival, S-wave arrival or neither (noise), respectively. A P or S prediction probability must exceed a threshold value of 0.4 to be identified as a true phase arrival detection (Lapins et al., 2021).

Events are then located using NonLinLoc, a probabilistic, nonlinear hypocenter location package (Lomax et al., 2000). The 1D starting velocity model used in the NonLinLoc inversion is based on the crustal structure of the Afar region deduced from wide-angle controlled-source seismology and assuming a V_P/V_S ratio of 1.76, the approximate average for continental crust (Ginzburg et al., 1981; Goitom, 2017). This produces an initial catalog of 31,387 events with at least four P-wave arrivals and one S-wave arrival that are available for subsequent use in seismic tomography inversions (Lapins et al., 2021).

2.2 Data Selection

Seismic tomography is highly reliant on accurate traveltime picks, and therefore we restrict the catalog produced by U-GPD and located in NonLinLoc based on the inversion statistics and event properties. We select earthquakes with at least four P and four S phases, azimuthal gaps that are less than 180° and location errors of less than 2 km, reducing the catalog to 11,319 earthquakes (Figure 1).

The U-GPD deep learning model does not include explicit pick uncertainties, but following Lapins (2021a), we associate errors to the picks based on the probability of being a true arrival. If this probability exceeds 0.85, a pick error of 0.05 s is assigned to it. Pick arrivals with probabilities 0.7 – 0.85, 0.55 – 0.7, and 0.4 – 0.55 are assigned pick errors of 0.1 s, 0.2 s, and 0.3 s, respectively. The tomography results are independent of the absolute values of these errors due to the application of regularization (see Section 3.4); rather, it is the relative difference in the pick errors that matters, giving less weight to the picks we are less confident in during the tomographic inversion.

3 Methodology

3.1 Tomographic Method

To investigate the subsurface velocity structure at Nabro, we make use of an iterative nonlinear tomographic inversion package, FMTOMO (Fast-Marching TOMOgraphy) (Rawlinson & Sambridge, 2004a, 2004b; de Kool et al., 2006). FMTOMO inverts seismic traveltime data to constrain 3D V_P and V_S structure. The package has been adapted by Pilia et al. (2013) to permit the fully nonlinear relocation of hypocenters and to solve directly for V_P/V_S structure. It has been applied in a variety of tectonic settings, using either passive or active source datasets, or a combination of the two (e.g., Rawlinson et al., 2006; Rawlinson & Kennett, 2008; Brikke, 2010; Pilia et al., 2013; Korger & Schlindwein, 2014; Zenonos et al., 2019; Wilks et al., 2020).

The key innovation of FMTOMO is the use of an efficient, consistent and robust grid-based eikonal solver known as the fast marching method (FMM) (Sethian, 1996; Sethian & Popovici, 1999) to solve the forward problem of predicting traveltimes in a 2D or 3D heterogeneous, layered medium. Since the subsurface structure beneath volcanoes is often highly heterogeneous, this makes FMTOMO an appropriate choice for our study of

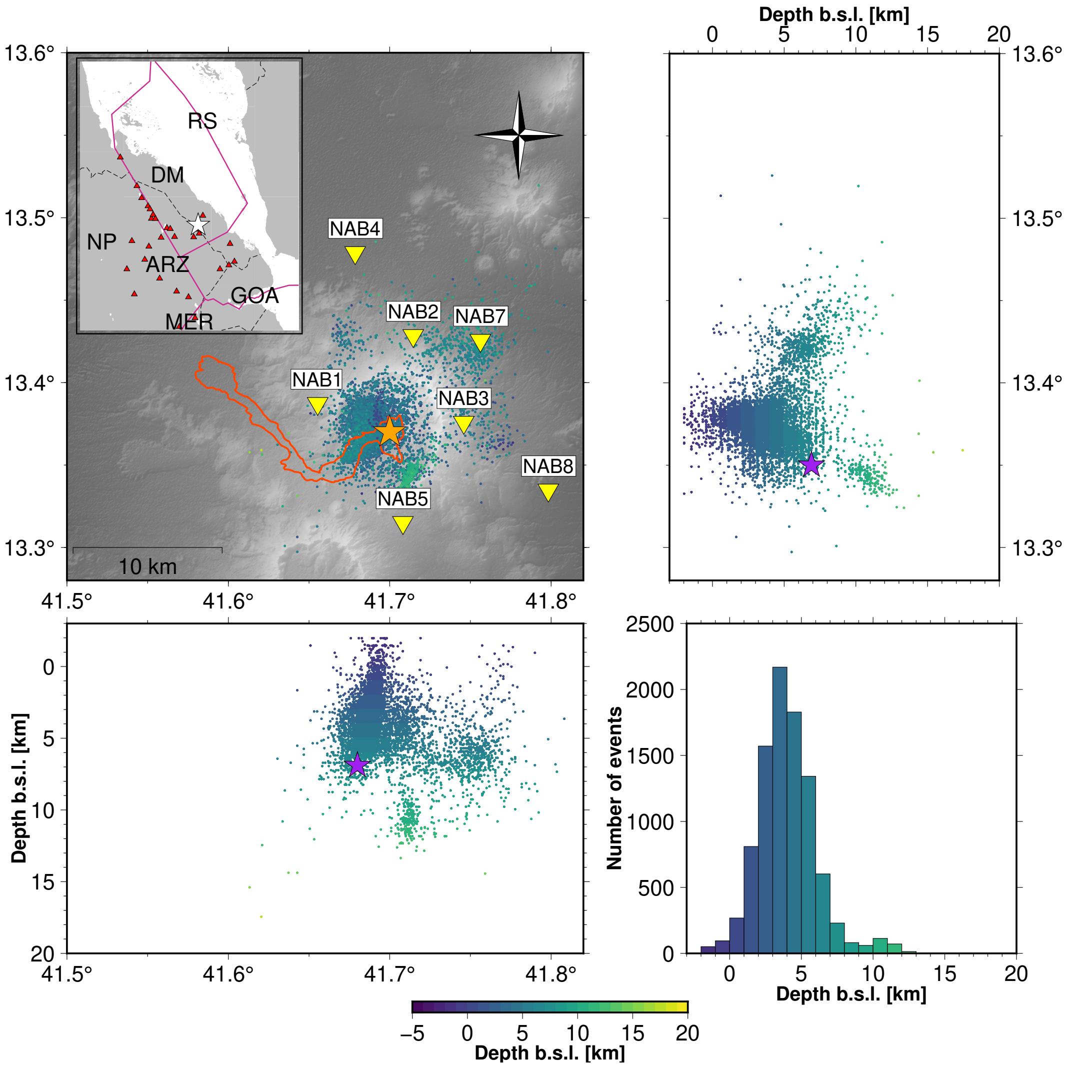

Figure 1. The final event catalog after relocation in a joint inversion for velocity structure and earthquake location. Thin black lines represent the caldera rims of Nabro and Mallahle calderas. Seismic stations from the temporary seismic network are plotted as inverted yellow triangles, excluding the inoperational station (NAB6). The dark orange line shows the extent of the 2011 eruption lava flow, and the orange star shows the location of the vent region (Hamlyn et al., 2014). The cross-sections show the catalog projected into the longitude-depth and latitude-depth planes, with the Mogi source from Hamlyn et al. (2014) represented by a purple star. The seismicity is coloured by depth below sea level (b.s.l.) and the histogram uses bins of 1 km depth b.s.l.. The inset shows a regional map of the Afar Triple Junction. Red triangles represent Holocene volcanoes recorded in the Smithsonian catalog 'Volcanoes of the World' database. The white star indicates the location of Nabro. Dashed lines are political borders. DM: Danakil Microplate, RS: Red Sea Rift, GOA: Gulf of Aden Rift, MER: Main Ethiopian Rift, ARZ: Afar Rift Zone, NP: Nubian Plate.

Nabro. Furthermore, FMTOMO can invoke traveltime reciprocity when solving the forward problem. The FMM source points are interchanged with the receivers, and the eikonal solver computes traveltimes from each receiver location to all the other grid points, so that the complete traveltime field for each receiver is available rather than for each source. Typically, most of the computing time of FMTOMO is dedicated to calculating these traveltime fields, and a large ratio between the number of sources and receivers means that invoking the reciprocity principle can lead to a significant increase in efficiency. We refer the reader to de Kool et al. (2006) for a more detailed overview of FMM.

FMTOMO defines the seismic velocity field with a regular 3D grid of nodes, which are used as the control vertices of a mosaic of cubic B-spline volume elements. Cubic B-spline functions preserve continuity of the second derivative whilst also being defined in terms of local basis functions, meaning that changing the velocity value of one node will only affect the velocities at nodes in the immediate vicinity. This creates a smoothly varying, locally-controlled velocity continuum. Cubic B-spline functions can also be rapidly evaluated, which is useful, since the multi-stage FMM requires several evaluations of the spline function.

The next step of the algorithm solves the linearized problem of matching observed and predicted traveltimes, i.e., finding model parameters that best satisfy the data. In this case, the data are the arrival time residuals, and the unknowns are the grid of vertices which control the pattern of the cubic B-spline velocity field. FMTOMO implements the gradient-based subspace inversion scheme of Kennett et al. (1988), which minimizes the objective function:

$$S(\mathbf{m}) = \frac{1}{2}\left[(\mathbf{g}(\mathbf{m}) - \mathbf{d}_{obs})^T \mathbf{C}_d^{-1} (\mathbf{g}(\mathbf{m}) - \mathbf{d}_{obs}) + \epsilon(\mathbf{m} - \mathbf{m}_0)^T \mathbf{C}_m^{-1} (\mathbf{m} - \mathbf{m}_0) + \eta \mathbf{m}^T \mathbf{D}^T \mathbf{m}\right], \tag{1}$$

where the vector $\mathbf{m}$ represents the model vector of unknown velocity parameters that are adjusted during the inversion process, $\mathbf{g}(\mathbf{m})$ are the predicted traveltime residuals associated with the model defined by $\mathbf{m}$, $\mathbf{d}_{obs}$ are the observed residuals, $\mathbf{m}_0$ is the reference model, $\mathbf{C}_d$ is the data covariance matrix and $\mathbf{C}_m$ is the *a priori* model covariance matrix. $S(\mathbf{m})$ is minimized when the model traveltimes most closely resemble the observed traveltimes. The subspace method locally minimizes the objective function by projecting the quadratic approximation of $S(\mathbf{m})$ onto an n-dimensional subspace of the full model space. In this case we choose a maximum of n = 20 orthogonal search directions, with singular value decomposition used to reduce the size of the subspace based on the magnitude of the singular values. Regularization constraints are applied to address solution non-uniqueness: the damping term encourages the search for models to remain within the vicinity of the reference model, whilst the smoothing term minimizes the amount of structural variation required to satisfy the observational constraint. Further information on the inversion scheme and how it is implemented can be found in Rawlinson et al. (2006).

Many local earthquake tomography algorithms rely on a linearized approach to the tomographic inversion (e.g., Evans et al., 1994). However, the hypocenter location problem is more strongly nonlinear than the velocity recovery problem, meaning that the linearized approximation leads to poor results in regions where there is significant velocity heterogeneity and/or where source locations are not well constrained (Pilia et al., 2013). Since the computational cost of having a fully nonlinear inversion scheme for both velocity structure and source location would be huge, we opt for a compromise approach using a fully nonlinear source relocation algorithm, which exploits the grid-based nature of FMM. The availability of the complete traveltime field for each receiver means that a fully nonlinear grid search for the best source location can be done efficiently, regardless of how complex the velocity model is (Pilia et al., 2013). The objective function minimized in the grid search is given in the Supplementary Information (Text S1).

Although the source relocation algorithm is fully nonlinear, the use of a linearised velocity inversion scheme means that an iterative approach is needed to account for the trade-off between velocity variations and hypocenter locations. The source and velocity inversions are done sequentially. Sources are first relocated using P- and S-arrival times via the nonlinear grid search method. Next, V_P and V_S are updated using the new locations, which involves two steps: 1) the solution of the forward problem using FMM; 2) an inversion for velocity parameters using the subspace inversion scheme. This is undertaken separately for P-wave and S-wave velocity structure, but both V_P and V_S models must be updated between each relocation as both P- and S-arrival times are used to constrain hypocenter location. We then repeat the entire process of source relocation and velocity inversion. In this case, an acceptable level of convergence is attained after six iterations.

Following this, we use the final hypocenter locations (as determined by the "joint" inversion for V_P, V_S and earthquake location) in the modified FMTOMO algorithm developed by Pilia et al. (2013) in order to calculate V_P/V_S. This procedure inverts S-P differential traveltimes for V_P/V_S structure along the ray paths from the S-wave model. We assume that 1) each S-wave path between two points has a corresponding P-wave path; 2) the P- and S-wave paths taken between two different points are identical and have similar Fresnel zones. Under these assumptions, the inverse problem is linear, as any lateral heterogeneity will cause a divergence of the P- and S-ray paths (Walck, 1988; Thurber, 1993; Eberhart-Phillips & Reyners, 2012). The method requires common P- and S-arrival times, so rays with only S-phases or P-phases will be removed. In our case, this does not result in significant data loss between the calculation of the V_P and V_S models as compared to the V_P/V_S model , as the U-GPD model phase association method has already discarded rays which only have S-arrivals (Lapins et al., 2021). See the Supplementary Information (Text S2) for more detail on how the problem is formulated within a linear framework, and Pilia et al. (2013) for a full description of the direct inversion of S-P differential traveltimes.

We choose to directly invert S-P differential traveltimes rather than dividing the P-wave model by the S-wave model to obtain V_P/V_S. S-wave data coverage tends to be poorer than P-wave data coverage, and is usually noisier, due to S-wave arrivals being more difficult to pick. The imposition of relatively arbitrary regularization constraints on the amplitude of anomalies means that the resulting S-wave solution models are comparatively smoother than P-wave models. For interpretation of individual P- and S-wave models, the absolute amplitude being correct is less relevant than the overall pattern of anomalies. However, when dividing the models to obtain V_P/V_S, the amplitude of P- and S-wave velocity anomalies directly influences the V_P/V_S model. If the S-wave model is smoother, the final V_P/V_S model obtained from direct division can inherit smaller wavelength features from the P-wave model, as shown by Pilia et al. (2013).

One potential drawback of our approach is that the V_P/V_S model cannot be derived explicitly from the V_P and V_S models but due to solution non-uniqueness, we argue that our inversion produces the optimum model of each type. Any inconsistencies must be viewed in the context of model uncertainty, which is unavoidable when undertaking an inversion with noisy data that is unevenly distributed. Indeed, synthetic tests show that the assumptions inherent to this technique have less effect on the results than ad hoc regularization choices (Pilia et al., 2013).

A flow chart detailing the full tomographic workflow can be found in the Supplementary Information (Supplementary Figure S10).

3.2 1D Model Selection

Under the assumption of weak nonlinearity, velocity perturbations cannot move too far from the unperturbed model. Hence, the starting reference model should ideally be as close to the true solution as possible to avoid the inversion becoming trapped in a local minimum that is far from the correct model. Initial test 3D inversions using a basic three-layer velocity model from Ginzburg et al. (1981) as a starting reference model do not resolve much detail, further demonstrating the need for a reference model that more closely reflects the local velocity structure at Nabro. Therefore we use FMTOMO in a 'quasi-1D' inversion to develop and refine a suitable 1D velocity model to use as a reference model for subsequent 3D inversions, following the method of Wilks (2016).

Because FMTOMO requires there to be at least two velocity grid nodes in any particular direction when the grid is defined, we cannot explicitly invert for 1D velocity structure. Instead, we perform 'quasi-1D' inversions using a simplified velocity grid, with two nodes defined in both latitude and longitude, spanning 13.15 – 13.55°N, 41.5 – 41.9°E. 23 nodes are defined in the depth direction, and the grid spans -3 km – 20 km b.s.l., resulting in velocities defined at $\sim$1 km depth increments. We then invert for V_P and V_S and relocate hypocenters, and calculate the average velocity at each nodal depth across the four nodes. FMTOMO automatically generates a boundary layer of two additional nodes at the grid limits, so it is important to exclude the nodes that make up this padding when averaging over the nodes.

When a velocity model with a number of discrete, homogeneous layers is used to locate earthquakes, they tend to cluster at the velocity discontinuities (Hamlyn et al., 2014). Thus we smooth out the sharp discontinuities in the three-layer regional model with a Gaussian filter and use the result as a starting model. The resulting P- and S-wave 'quasi-1D' velocity models are plotted in Figure 2.

For the P-wave velocity inversion, the data variance is reduced from 0.0997 s^2 to 0.0273 s^2. For the S-wave velocity inversion, the variance is reduced from 0.264 s^2 to 0.0469 s^2. This suggests that this new 1D model is 'closer' to the solution model and represents the seismic structure at Nabro more accurately than the three-layer regional model from Ginzburg et al. (1981).

To investigate how sensitive the 3D solution model is to the initial model, we perturb each value of the new 1D model randomly by up to 10% prior to inversion and carry out 3D tomographic inversions. We find that the solution models show broadly similar structure, with differences only occurring outside of the data resolution limits determined by synthetic resolution tests described in Section 4 (i.e., the models differ in small-scale structure or in regions of poor data coverage). Results of these perturbation tests are plotted in Supplementary Figure S1 and described in the Supplementary Information (Text S3). Analysis of the inversion statistics shows the same or higher traveltime residuals and variances for the solution models using the perturbed 1D model compared to their starting model, as expected, with percentage deviations that are less than 16% as shown in Supplementary Table S1. Therefore we conclude that our choice of 1D starting models is robust, and use these models as the starting model in all of the subsequent V_P and V_S 3D inversions.

3.3 Defining a Grid for 3D Inversions

Before undertaking 3D inversions, we first define an inversion grid, which describes the velocity model in terms of cubic B-spline functions. We also define a propagation grid, which represents a discrete sampling of the velocity field for use in the grid-based eikonal solver employed during the forward step and during the nonlinear relocation of events. Both grids are comprised of a 3D set of nodes that span 13.15°N – 13.55°N, 41.5°E – 41.9 °E, and -3.0 km – 20.0 km in depth below sea level. The node spacing for the propagation grid is chosen to be $\sim$0.5 km and for the inversion grid it is $\sim$1 km. The relocation code also carries out a sub-cell search, dicing the initial cells by a factor of 10, and therefore 50 m is the smallest separation distance between the relocated earthquakes. The inversion grid spacing is sufficiently small to capture features that are constrained

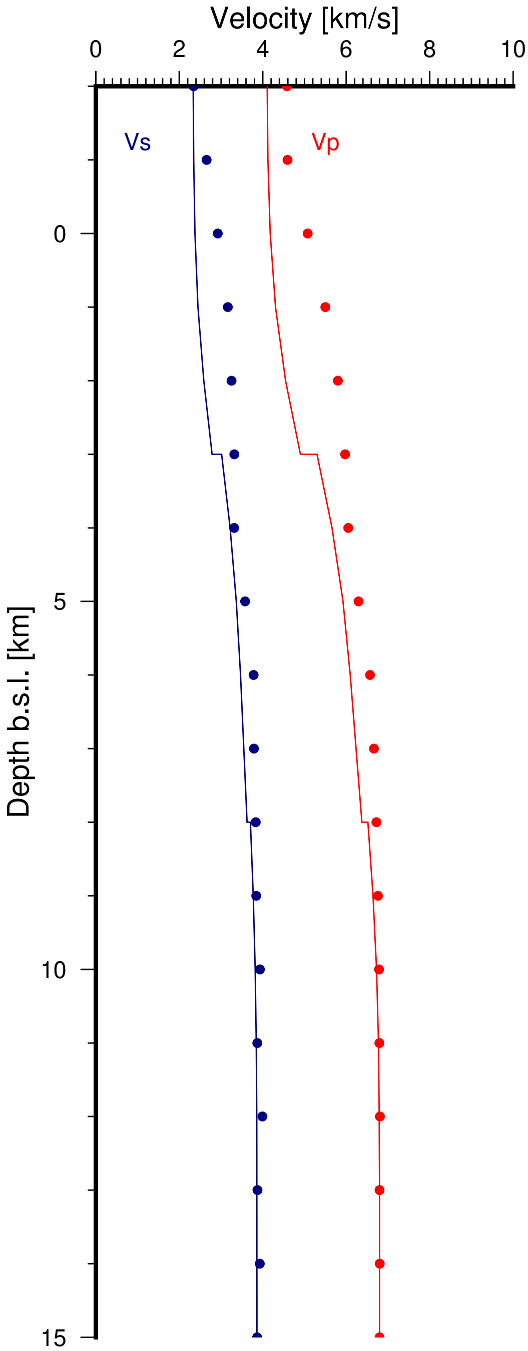

Figure 2. The V_P and V_S velocity model output from a quasi-1D inversion (red circles and navy circles respectively), compared with the smoothed 3-layer starting models (red and navy lines respectively.

by the data, noting that smoothing is applied to control the wavelength of recovered features. At half the spacing of the inversion grid, the propagation grid is sufficiently fine to render errors in the forward prediction of traveltimes sufficiently small that they will not influence the inversion results. The 1D model determined in Section 3.2 is used as a starting model.

3.4 Optimising Data-Model Fit

The aim of the tomographic inversion procedure is to find a model that is similarly smooth and as close to the initial model as possible (to satisfy local linearity), whilst still satisfying the data. Therefore, three parameters need to be minimized: data fit, model variance and model roughness. The solution model variance is a measure of the difference between the starting model and the final model, and model roughness is a measure of how much complexity exists in the final model itself (based on the second spatial derivative). We optimise these using the smoothing and damping parameters, η and ϵ. These regularization parameters also affect the data fit, i.e., the difference between the observed data and the final solution model predictions, quantified by the variance of the traveltime residuals.

Through numerous inversions for 3D velocity structure using different values of the regularization parameters, we plot trade-off curves to find the damping and smoothing parameters that give the best compromise between data fit, model variance and model roughness. This process is done separately for the V_P, V_S and V_P/V_S models; see the Supplementary Information (Text S4) for further detail. For V_P the parameters are $\epsilon = 3$ and $\eta = 10$, for V_S they are $\epsilon = 10$ and $\eta = 50$ and for V_P/V_S, $\epsilon = 100$ and $\eta = 20$ (see Supplementary Figure S2).

3.5 Earthquake Relocations

After an initial inversion using the optimal damping and smoothing parameters, we examine the output relocated seismicity, plotted in Supplementary Figure S3. We find that many events have been relocated substantial distances. A considerable number of earthquakes migrate to the inversion grid boundaries and above the topography line, which indicates that the initial locations of these earthquakes are poorly constrained. The mean relocation offset is 1.61 km. Therefore, we identify events that are relocated by distances greater than 3 km, and remove them from the catalog. We then repeat the inversion procedure with this reduced catalog of 8,893 events in order to improve the inversion stability.

The inversion results using the new subset of events show improved data fits over the full catalog. For V_P the data variance of the final solution model is reduced from 0.0218 s^2 using the full catalog to 0.0101 s^2 using the subset of events. The data variance of the final V_S solution model decreases from 0.0298 s^2 to 0.0170 s^2. V_P/V_S also experiences a reduction in the variance from 0.0386 s^2 to 0.0283 s^2. Furthermore, events are now relocated by reduced offsets: the mean relocation offset for the reduced catalog is 0.91 km. We note that some earthquakes remain located above the topography line after this process. We attribute this to shallow events being more poorly constrained and thus erroneously relocated in the air. The average depth uncertainty across all events located above sea level is $\pm$4.99 km, calculated following Wilks et al. (2020)and described in the Supplementary Information (Text S1). The shallowest depth an earthquake is relocated to is 2.49 km above sea level. Therefore, within error, the location of these earthquakes is consistent with their true locations being in the very shallow subsurface.

We therefore use this reduced catalog in the following section to carry out resolution tests and produce the final solution model.

4 Results

4.1 Checkerboard Resolution Tests

The tomographic inversion problem is non-unique, with many different models able to satisfy the data. Different factors that help constrain the solution of this inverse problem include the path coverage of the data, data noise and the choice of implicit and explicit regularization. Thus, assessing the solution robustness is challenging, yet crucial for comprehensive evaluation of the spatial resolution of the estimated model.

Synthetic reconstruction tests are typically used to investigate the robustness of tomographic models. During these tests, a heterogeneous synthetic model is formulated and the forward problem is solved using this model, with the identical source-receiver configurations to the observational dataset. This produces a synthetic traveltime dataset. The same inversion method used for the experimental data is applied to the synthetic dataset in order to reconstruct the synthetic model. The most common input structure is a 'checkerboard' structure overlain on the starting model, with alternating positive and negative velocity anomalies making up the 'checkers' (e.g., Hearn & Clayton, 1986; Glahn et al., 1993; Rawlinson et al., 2003). Regions where the checkerboard pattern is recovered are considered to be well resolved.

The parameters we choose for our checkerboard tests are: $\mathrm{V_P}$ perturbations set to ± 0.5 km/s from the initial model ($\pm 7.35-11.7\%$) and $\mathrm{V_S}$ perturbations set to ± 0.2 km/s from the initial model ($\pm 5.18-8.69\%$). It is instructive to generate checkerboards with different scale lengths of perturbation—this amounts to altering the number of grid nodes, N, that are perturbed simultaneously. For example, a checkerboard of size $N = 2$ will have nodes perturbed in pairs. Increasing the value of N will increase the size of each checkerboard element. In Figure 3, we present checkerboard tests with size $N = 2, 4, 8$, corresponding to scale lengths of ∼2 km, ∼4 km and ∼8 km respectively, to assess the model resolution at different scales.

If no noise is added to the synthetic dataset, the result will give an indication of the optimal spatial resolution. However, since data noise is present in all seismic datasets, noise with a Gaussian distribution is often added, with a standard deviation equal to that of noise estimates obtained from the data. However, it is important to note that estimating data uncertainty is often subjective, and it is not clear that the actual noise distribution takes a Gaussian form (Rawlinson & Spakman, 2016). Bearing this in mind, we add Gaussian noise with a standard deviation of 0.05s, representing half a cycle of the dominant frequency of the microseisms (∼10 Hz).

For our synthetic checkerboard test, we carry out six iterations for $\mathrm{V_P/V_S}$ and source location, with results plotted in Figure 4. The output checkerboards of scale length ∼4 km and ∼8 km show that $\mathrm{V_P/V_S}$ anomalies on these scales are well-resolved within the seismic network in map view (Figure 4a and b). Both checkerboards are resolvable down to 10 km depth b.s.l.. The finest scale checkerboard (∼2 km, Figure 4c) is much less well-defined.

These tests indicate the limits of resolution of our dataset—they demonstrate that $\mathrm{V_P/V_S}$ anomalies can be robustly detected above depths of 10 km within the seismic array and on scale lengths greater than ∼2 km. Similar resolution is observed in the results of synthetic inversions for $\mathrm{V_P}$ and $\mathrm{V_S}$ structure (see Supplementary Figures S5 and S7 and Text S5).

The lack of recovery of anomalies at depth can be explained by 99% of the seismic events in our dataset occurring between the surface and ∼10 km depth b.s.l.; thus, there are very few paths available to resolve structure below this depth. The amplitude recovery of the input perturbations varies–in places the amplitude of anomalies is underestimated, whereas it is overestimated in certain regions (e.g., the negative anomaly in the longitude cross-section of Figure 4a). Outside the seismic array, the amplitude recovery is particularly weak, as expected.

4.2 Inverting for 3D Velocity Structure

4.2.1 Inversion Statistics

Table 1. Inversion Statistics for the Final V_P, V_S and V_P/V_S Inversions

RMS residuals			
Parameter	**Starting model**	**Solution model**	**Reduction (%)**
V_P	0.166 s	0.104 s	37.3
V_S	0.182 s	0.130 s	28.6
V_P/V_S	0.192	0.168	12.5
Variance			
Parameter	**Starting model**	**Solution model**	**Reduction (%)**
V_P	0.0276 s^2	0.0110 s^2	60.1
V_S	0.0332 s^2	0.0170 s^2	48.8
V_P/V_S	0.0364	0.0283	22.3
χ^2			
Parameter	**Starting model**	**Solution model**	**Reduction (%)**
V_P	4.59	1.39	69.7
V_S	9.60	4.66	51.5

The inversion statistics in Table 1 show that the RMS arrival time residuals and the data variance are reduced for the final P-wave, S-wave and V_P/V_S solution models as compared to the starting models. The normalized χ^2 value is the result of a statistical test for how well a model compares to actual observed data. In theory, it should be equal to 1 if all the data are satisfied to the level of the noise. For the V_P solution model, it is reduced to $\chi^2 \approx 1$, but for V_S it is only reduced to $\chi^2 = 4.66$. However, as detailed by Rawlinson et al. (2010), tomographic inversions usually do not have $\chi^2 = 1$ due to a) estimation of data uncertainties being difficult to quantify; b) the use of a regular and smooth model parameterisation; c) application of *ad hoc* regularization to stabilize the inversion, which suppresses some structures that are needed to satisfy the data; d) the assumptions and approximations made when solving the forward problem. Thus the range of models that can be retrieved is limited. Despite this, the final data fit is a significant improvement on the starting 1D models for all the solution models, indicating that recovered lateral heterogeneities are generally required by the data and hence are physically meaningful within the limits of data resolution, as estimated from the synthetic tests.

4.2.2 Velocity Structure

Figure 5 shows east-west and north-south cross-sections through the final V_P, V_S and V_P/V_S solution models. The cross-sections are taken through the center of the caldera, passing directly through the vent location of the 2011 eruption (Hamlyn et al., 2014). For clarity, we only plot the anomalies and seismicity below the topography line. The

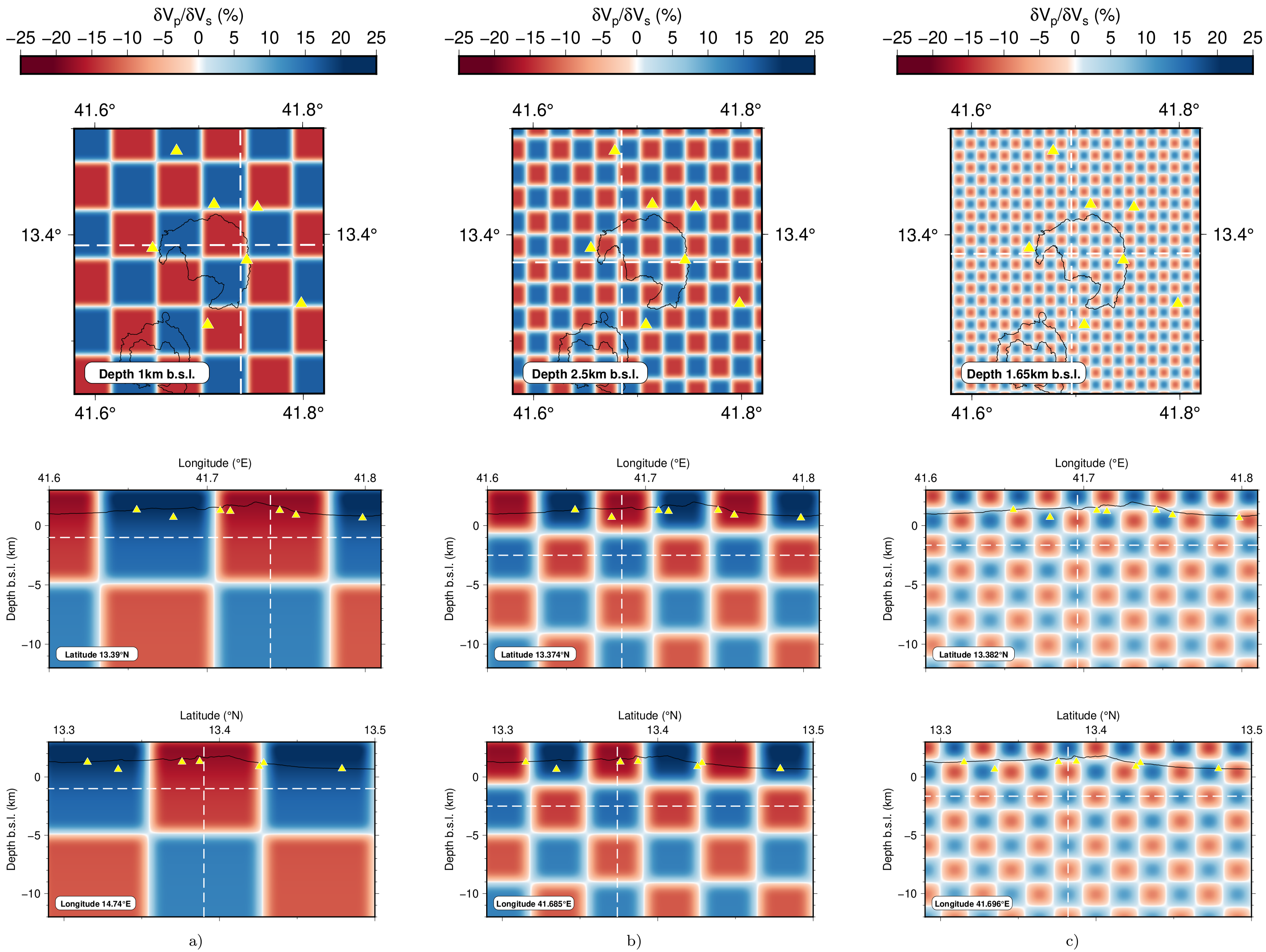

Figure 3. Input V_P/V_S checkerboard models of differing scale lengths: a) ∼8 km; b) ∼4 km; c) ∼2 km. Slices are taken through the maximum perturbations of each checkerboard in latitude, longitude and depth, as indicated by the white dashed lines. Seismic stations are plotted as yellow triangles.

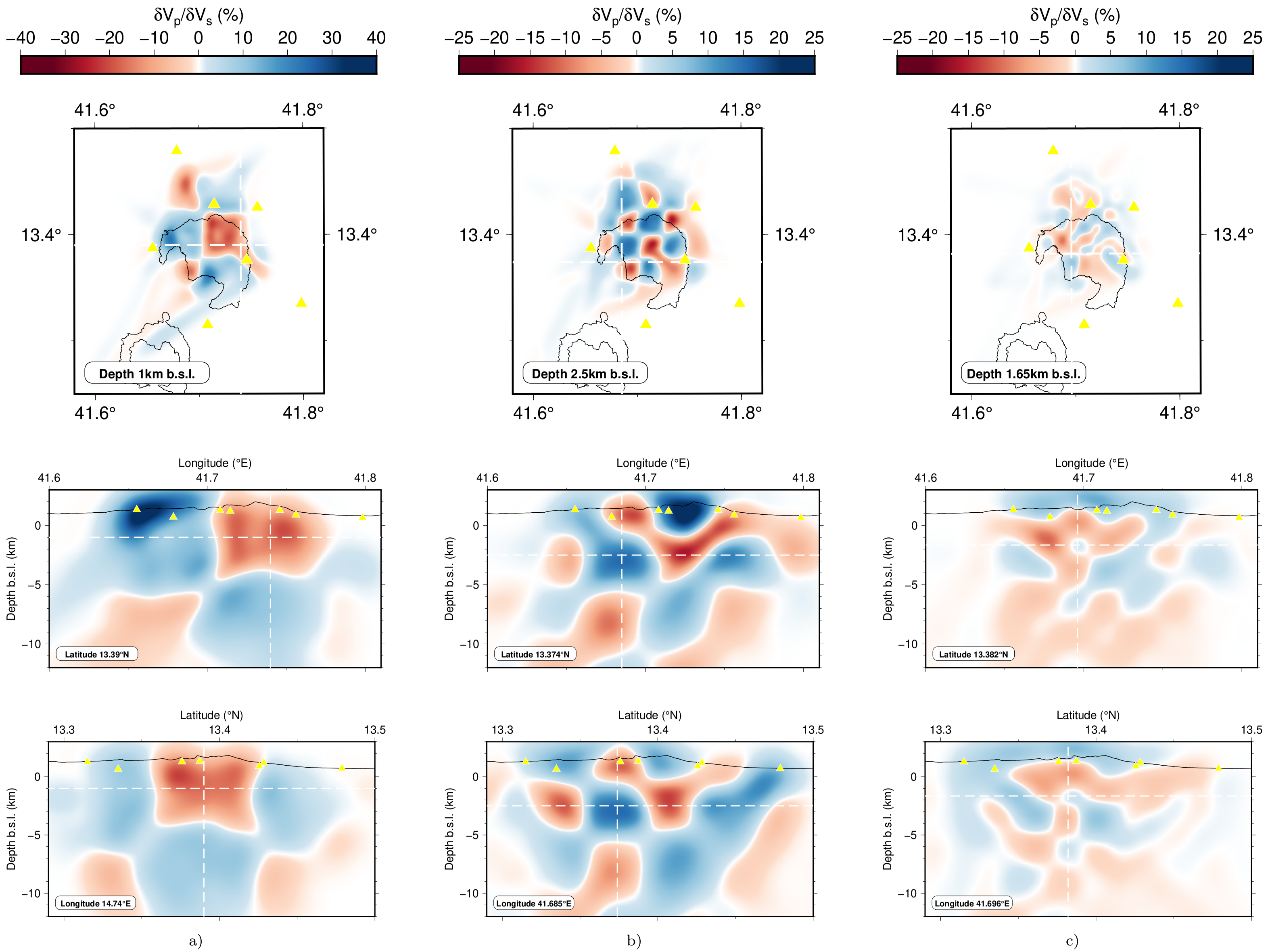

Figure 4. Output V_P/V_S checkerboard models of differing scale lengths: a) ~8 km; b) ~4 km; c) ~2 km. Slices are taken through the maximum perturbations of each checkerboard in latitude, longitude and depth, as indicated by the white dashed lines. Seismic stations are plotted as yellow triangles.

original figures can be seen in the Supplementary Information (Supplementary Figure S8). Depth slices are plotted in Figure 6.

The dominant feature in the V_S solution model (Figure 5c–d, Figure 6e–h) is a region of high V_S and high levels of seismicity within the caldera outline, extending downwards from the surface to 6 km b.s.l.. At 6 km b.s.l., an aseismic region of low V_S is observed, extending downwards to $\sim$ 10 km b.s.l.. Close to the surface, the high V_S region is surrounded to the north and south by very low V_S areas, and to the east and west by less pronounced low V_S areas, all of which are aseismic.

The V_P model shows more heterogeneity compared to the V_S model. The difference is particularly noticeable in the perpendicular east-west and north-south cross-sections taken through the center of the caldera (Figure 5a–b). A low V_P structure extending from 41.7 – 41.8°E dips from east to west from a depth of 4 km b.s.l. to 10 km b.s.l.. Above this, there is a region of high V_P. This region contains two low V_P anomalies extending $\sim$ 2–3 km in depth and $\sim$0.2° in longitude, which is around the limit of data resolution. In the depth slice at 1 km b.s.l., a low V_P region extends from 13.44 – 13.48°N, aligned N-S (Figure 6a). This region extends in depth down to 10 km b.s.l., as observed in the longitude cross-section (Figure 5a), and is seismically active.

Following the joint inversion for V_P and V_S structure, we calculate the average ratio of the V_P and V_S models across all velocity grid nodes, which is 1.77. We use this reference value to adjust our colour scale in the V_P/V_S plots in Figures 5 and 6; red colours correspond to ratios higher than the reference and blue colours to ratios lower than the reference.

At depths of 6–10 km b.s.l., a region of high V_P/V_S ratio (as high as 1.9) is observed in the longitude and latitude cross-sections (Figure 5e–f). This region correlates with low V_S and low V_P anomalies, and is aseismic. Above this high V_P/V_S region, there is an area of high seismicity and very low V_P/V_S ratio (as low as 1.5), extending from depth 0 km b.s.l. down to 6 km b.s.l. and lying within the caldera outline (Figure 6i–l). The strongest low V_P/V_S ratios are seen between 0–2 km b.s.l. and correspond to high V_S values. Close to the surface, high V_P/V_S ratios are observed again, with the ratio reaching 2.0 in places. These high V_P/V_S regions all exhibit low levels of seismicity.

As described in Section 3, we obtain the V_P/V_S solution model by directing inverting S-P differential traveltimes. We also plot the solution model obtained from simply dividing the V_P solution model by the V_S solution model (Supplementary Figure S9). The direct division model shows largely the same pattern of velocity anomalies within the data resolution limits determined by our synthetic tests (Section 4). Differences in amplitude are seen, but this is expected due to solution non-uniqueness and the imposition of regularization constraints. Thus, we are confident that our method produces a model that is consistent with direct division, and that our subsequent interpretations of these V_P/V_S ratio anomalies would remain the same if we had chosen to directly divide the V_P solution model by the V_S solution model instead.

5 Discussion

5.1 Defining a Local 1D Velocity Model at Nabro

Compared to the three-layer velocity model developed for the Afar region in previous studies, our refined local 1D velocity model has faster P- and S-wave velocities in the uppermost 10 km. High crustal velocities in a volcanic setting are typically attributed to the presence of solidified, high-strength intrusive magmatic rocks, such as the cumulates and dykes at Mount Etna (Aloisi et al., 2002), a plutonic body at Mount St. Helens (Lees, 1992), an old lateral dyke system at Tungurahua volcano (Molina et al., 2005) and the solid andesitic cores of the volcanic complexes of Soufriére and Centre Hills, Montser-

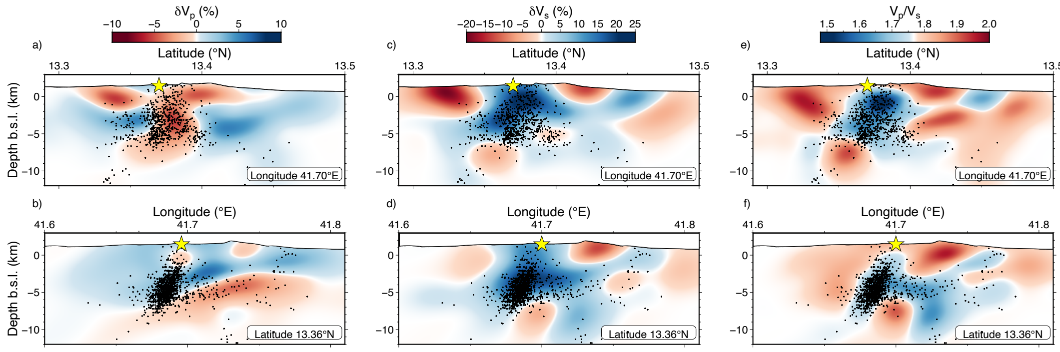

Figure 5. Cross-sections through the final V_P (a, d), V_S (b, e) and V_P/V_S (c, f) solution models at a longitude of 41.7°E and latitude of 13.36°N (the center of the caldera). The V_P and V_S models are plotted as percentage deviations from the initial 1D model. The V_P/V_S ratio model is plotted as absolute values, with the center of the colour bar corresponding to the reference V_P/V_S value–the average ratio of the V_P and V_S models across all velocity grid nodes. Earthquakes within ±1 km of the displayed section are indicated by black dots. The yellow stars mark the vent location of the 2011 eruption. As discussed in the text, we only show the earthquakes and anomalies below the topography line for the purposes of clarity, with the full solution plotted in Supplementary Figure S8.

rat (Paulatto et al., 2010; Shalev et al., 2010). At Nabro, analysis of inclusions in erupted products from 2011 suggests that these are derived from older and more primitive basalt (Donovan et al., 2018). The presence of xenocryst material in the erupted magmas leads Donovan et al. (2018) to conclude that the subsurface crustal structure beneath the caldera is composed of a series of sills and older eruptive products. This provides supporting evidence that the elevated crustal velocities directly beneath Nabro reflect intrusions, potentially remnants of earlier episodes of magmatism.

Below 10 km, the refined model shows negligible variation from the regional model, as expected due to the fact that the vast majority of seismic events originate above 10 km b.s.l.. Using this refined local 1D model as the starting model for tomographic inversions results in solution models that better fit the traveltime data.

5.2 Earthquake Detection Using U-GPD

This study presents the first seismic tomography results from an earthquake catalog detected using machine learning methods. The inversion statistics from this study (RMS residuals, variance and χ^2) are of the same order of magnitude as those from previous FMTOMO studies that relied on manually picked catalogs of earthquakes (e.g., Wilks et al., 2020; Pilia et al., 2013), demonstrating that our use of the deep learning model U-GPD to pick the seismic arrivals has not adversely affected the stability and robustness of the inversion. The method therefore has the ability to detect seismic events with sufficient accuracy to be used successfully in an FMTOMO tomographic inversion. This has implications for future tomographic studies at volcanoes: the efficiency of U-GPD's phase arrival picking method means that far more events can be detected than previously possible, enabling more timely exploitation of such data for the purposes of seismic tomography.

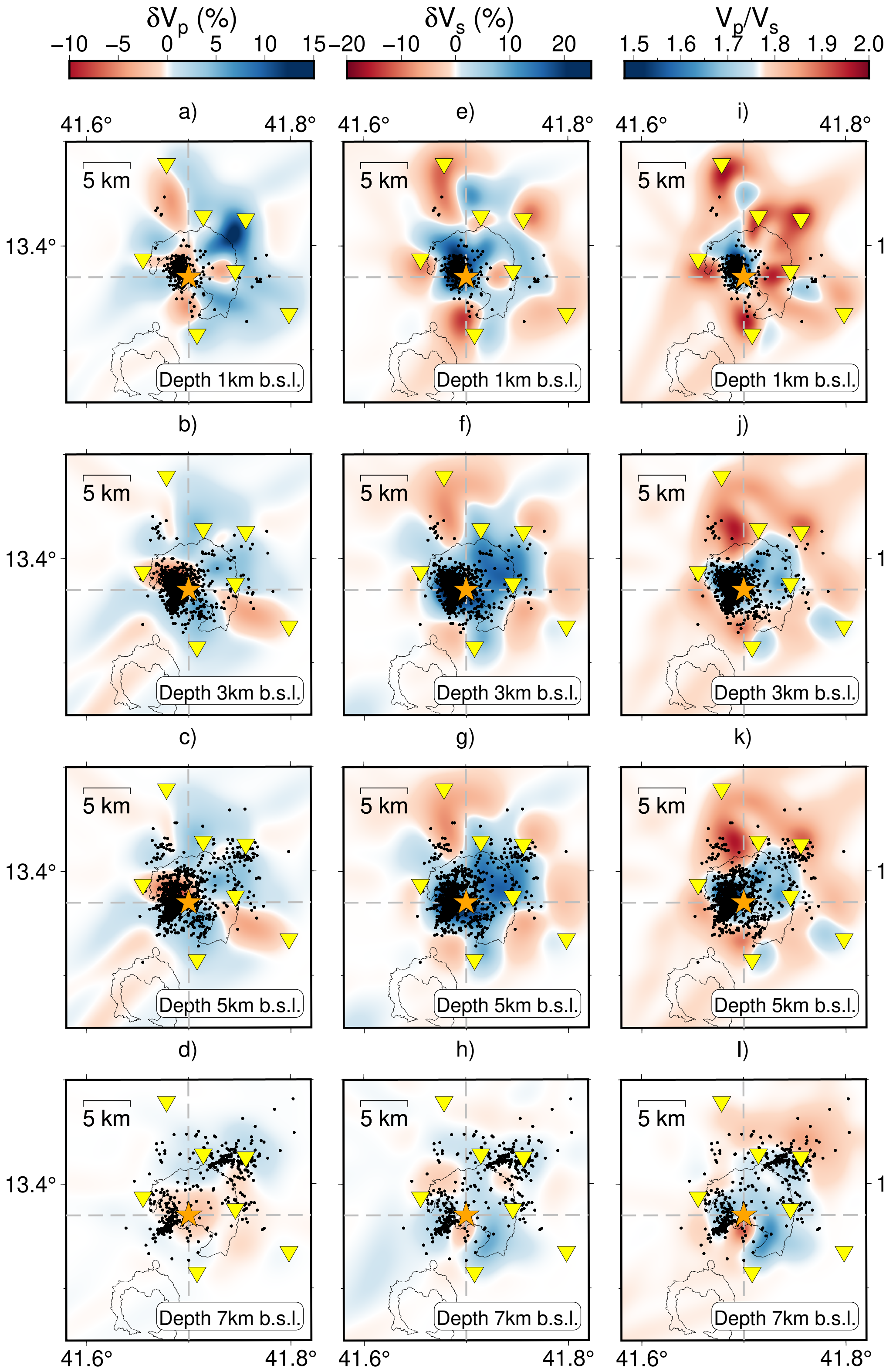

Figure 6. Cross sections at depths of 1km, 3 km, 5 km and 7 km below sea level (b.s.l.) through the final (a–d) V_P, (e–h) V_S, and (i–l) V_P/V_S ratio velocity models. The V_P and V_S models are plotted as percentage deviations from the initial 1D model. The V_P/V_S ratio model is plotted as absolute values, with the center of the colour bar corresponding to the reference V_P/V_S value–the average ratio of the V_P and V_S models across all velocity grid nodes. Earthquakes within ±0.5 km of the displayed section are plotted as black dots and seismic stations are plotted as yellow inverted triangles. The orange stars mark the vent location of the 2011 eruption. The grey dashed lines represent the latitude and longitude cross-sections depicted in Figure 5.

5.3 Interpretation of V_P/V_S Variations

Seismic velocity variations reflect a variety of physical parameters, including rock characteristics (composition, porosity, fractures, mineralogy), saturation conditions, presence of fluids (gases or liquids), temperature, and pressure. The interplay of these diverse influences makes it difficult to interpret observed seismic anomalies. Considering the ratio of compressional velocity to shear velocity, V_P/V_S, enables greater constraint to be placed on the cause of seismic velocity variations. This is particularly helpful when attempting to constrain the location of fluids in the subsurface of a volcano, because the V_P/V_S ratio is sensitive to the type of fluid present and can distinguish between regions of partial melt or hydrothermal fluids, both of which are encountered beneath volcanoes. In saturated or partially-saturated rocks, the content and physical state of fluids has a greater effect on P-wave velocities than S-wave velocities (Vanorio et al., 2005). Fluid phase transitions induce changes in fluid compressibility and thus bulk modulus (Ito et al., 1979; Wang & Nur, 1986). Shear moduli are little affected by fluid phase transitions and hence S-wave velocities change insignificantly due to a density effect, meaning that low V_P/V_S ratios tend to characterize gas-bearing rocks (i.e., those with high fluid compressibility) whereas liquid-bearing rocks (with low fluid compressibility) are characterized by high V_P/V_S ratios (Vanorio et al., 2005).

5.3.1 High V_P/V_S *Anomaly at 6–10 km Depth*

In Figure 5, the high V_P/V_S (> 1.9) region at 6–10 km b.s.l. coincides with pronounced low V_S ($< 3.8kms^{-1}$)and low V_P ($\sim 6.6\ kms^{-1}$) anomalies as compared to the starting model. This correlation between the P- and S-wave velocity models in a region of high V_P/V_S ratio suggests a region of elevated temperature (Sanders et al., 1995). Furthermore, the anomalous region is approximately aseismic. In an examination of a deep cluster of seismicity at Nabro, Lapins (2021a) finds that the highest attenuation is observed at station NAB1 where the raypaths travel directly through this aseismic, high V_P/V_S anomaly, suggesting that the region attenuates S-waves strongly. Anomalously low Q_S at depth is usually attributed to the presence of partial melt (Sanders et al., 1995). The region also coincides with the location of a Mogi source inferred by Hamlyn et al. (2014) to explain the observed post-eruptive surface subsidence at Nabro. Petrological analysis by Donovan et al. (2018) finds that most melt inclusions in erupted products from the 2011 eruption were entrapped at 5–10 km depth b.s.l.. This represents the storage location of an older body of melt which was remobilized and erupted when an intrusion of fresh melt rose through the crust and mingled with the older melt (Donovan et al., 2018). The estimated depth of this melt body is consistent with the depth of our observed high V_P/V_S anomaly.

Previous tomographic studies at volcanoes have interpreted similar regions with high V_P/V_S ratios as delineating magmatic storage zones. For example, an anomalous body with low P-wave velocity, low S-wave velocity and V_P/V_S ratio > 1.84 is observed by Lin et al. (2014) at 8–11 km depth beneath the Kīlauea volcano in Hawaii, and interpreted as a crustal magma reservoir beneath the volcanic pile. At Nevado del Ruiz volcano in Colombia, a region of high V_P/V_S ratios (> 1.80) at 2–10 km is inferred to be an intrusive body of magmatic origin that included partial melt zones associated with low S-wave velocity anomalies (Londoño & Sudo, 2003). Greenfield et al. (2016) observe a pair of prominent anomalies with low P- and S-wave velocities and V_P/V_S ratios $>$ 1.82 at depths of 5 km and 9 km b.s.l. beneath Askja volcano, Iceland, which are interpreted as the primary magma storage regions in the upper crust.

Thus, we interpret the high V_P/V_S anomaly as the storage location of melt that fed the 2011 eruption. Only a small fraction (5–20%) of the stored melt is typically erupted at the surface (Greenfield & White, 2015; White et al., 2019). This is seen in the results of a post-eruption seismic velocity study at Mount St. Helens, which finds that there is a persistent high V_P/V_S region at 4–13 km b.s.l., interpreted as the primary upper-middle crustal magma reservoir and indicating that a significant amount of melt remains in the crust (Kiser et al., 2016). Similarly, our observation of a high V_P/V_S region at depths 6–10 km b.s.l. suggests that melt is still stored at these depths, which could feed future eruptions.

5.3.2 Low V_P/V_S *Region*

Above the inferred magma storage region, our results show a region of low V_P/V_S ratio (1.5–1.7), colocated with high S-wave velocities ($> 3.6kms^{-1}$) and low P-wave velocities compared to the starting model (region B in Figure 7). This anomaly extends from depths of $\sim$ 5 km b.s.l. to the surface. The high V_S values can be explained by lithology—high-strength, solidified intrusive magmatic rocks are expected to show high seismic velocities (e.g., Lees, 1992; Aloisi et al., 2002; Molina et al., 2005; Lees, 2007). However, the V_P/V_S ratio in intrusive igneous rocks is expected to be higher than typical continental crust (Christensen, 1996), whereas the V_P/V_S ratio we measure in this region is low—down to 1.5 in places—and so there must be another factor acting to reduce the V_P/V_S ratio. It has been shown that the velocities of P- and S-waves in rocks are strongly affected by the saturation conditions of the rock, particularly whether the rock is saturated with gas, liquid or a mixture thereof (Toksöz et al., 1976; Ito et al., 1979). A geothermal regime near the water-steam transition has low P-wave velocities but normal S-wave velocities: the presence of gas reduces the bulk modulus and causes a decrease in P-wave velocity, without significantly altering the propagation of shear waves (Walck, 1988). The addition of a small amount of gas in a water-brine mixture can lower the velocity of P-waves significantly (Toksöz et al., 1976). We observe low P-wave velocities coincident with the lowest V_P/V_S ratio in our model, providing evidence for the presence of gas in the rocks in this region. Furthermore, calculations of seismic attenuation in P- and S-waves at Nabro show that P-wave attenuation is significantly higher than S-wave attenuation across all seismic stations (Lapins, 2021a), which is generally attributed to partial saturation of a compressible fluid in cracks, fractures or pores (Winkler & Nur, 1979; Hauksson & Shearer, 2006; Amalokwu et al., 2014). Further evidence in support of the existence of gases in the upper subsurface is the significant post-eruption fumarolic activity observed at Nabro (Yohannes, 2012). Petrological analysis of melt inclusions erupted in 2011 indicates that melt-fluid separation occurred at depths of up to 18 km b.s.l., generating CO_2 rich fluids (Donovan et al., 2018). The magma storage zone described in Section 5.3.1 coincides with a Mogi source; the deformation model invokes deflation, which is explained by the outgassing of magma at depth (Hamlyn et al., 2018). The low V_P/V_S region could reflect the degassing pathways between the magma and the surface fumaroles.

A velocity reversal is seen in the 1D V_S model between 3–4 km b.s.l., where velocity values decrease with depth (Figure 2). The trend in V_P does not reverse here, but the rate of change of velocity with depth decreases. The location of these reversals is coincident with the lowest V_P/V_S ratio seen in the model. Density, resistivity and sonic velocity logs that go through velocity reversals are generally interpreted as departures of the effective stress from normal compaction trends (Hottmann & Johnson, 1965; Pikington, 1988; Bowers, 2002). Overpressure is one explanation for this. If the fluid pressure is higher than the normal hydrostatic fluid gradient for a given depth, it prevents the effective stress from increasing with depth as it usually would (Vanorio et al., 2005). To be over-pressurized, the gas present in the low V_P/V_S region would have to be trapped and experiencing expansion, uplift, compaction, temperature increase or a combination of these factors; all of which are possible in the context of a recently active volcano. Indeed, the overpressure could be driven by the magma storage zone directly below the low V_P/V_S region that extends from depths of $\sim$ 5 km b.s.l. to the surface (Hamlyn et al., 2018).

Nabro's caldera outline matches the region of high V_S and low V_P/V_S well (Figure 6), while the low V_P region is slightly smaller. Therefore, we propose that the crustal structure within the caldera is formed of intrusive rock, potentially with layers of stacked sills from previous eruptions. This would elevate the S-wave velocity.

During the June 2011 eruption of Nabro, magma ascended to the surface via a NW-SE-oriented dyke (Goitom et al., 2015). Volcanic conduits have associated damage zones, common to all shallow magmatic systems beneath volcanoes (Afanasyev et al., 2018), and contain fragmental infills related to prior intrusions, eruptions and steam explosions (Blundy et al., 2021). These conduits therefore have high porosities, within which fluids can be stored. Dyke emplacement also causes fracturing and creates permeable pathways for fluid transport and accumulation (e.g., Bakker et al., 2016; Brown et al., 2007). Our results show that this region is highly seismogenic, pointing to the presence of fractures and cracks enabling fluid migration that drives pore pressure increases and leads to abundant seismicity. Thus, the most likely route from the degassing magma storage region to the surface is along the conduit that fed the 2011 eruption, as it will be formed from highly permeable and damaged rock. This explains why the low V_P region (indicating the presence of gas) is less horizontally extensive than the high V_S region.

Similar conclusions are reached at Aluto volcano, where a region of low V_P/V_S ratio is interpreted as the signature of an over-pressurized gas volume within a hydrothermal system (Wilks et al., 2017, 2020). A seismogenic zone of low V_P/V_S ratios coincident with low P-wave velocities is also observed at Campi Flegrei, and explained as over-pressurized gases accumulating at the top of dyke intrusions (Vanorio et al., 2005; Chiarabba & Moretti, 2006). At Nevado del Ruiz volcano, the upper part of a high P- and S-wave velocity anomaly (0–2 km depth) is characterized by low V_P/V_S ratios (< 1.68) and described as a steam-dominated geothermal system by Londoño and Sudo (2003). Multiple studies of Mammoth Mountain, California, have identified a low V_P/V_S region from depths of -3–2 km, attributed to the presence of CO_2 distributed in oblate spheroid pores, which supplies gas-rich thermal springs at the surface (Julian et al., 1998; Foulger et al., 2003; Lin, 2013; Dawson et al., 2016).

Our observations have shown that the degassing of partial melt influences the upper crustal substructure beneath Nabro. The coupling of the shallow heat source to volatile transport above, as well as the presence of fumaroles at the surface, suggests the possibility of a high-temperature geothermal system similar to those hosted by volcanic s in the Main Ethiopian Rift (Pürschel et al., 2013).

5.3.3 Shallow, High V_P/V_S Anomalies

In volcanic settings, high V_P/V_S values at depth are typically associated with the presence of melt. However, the high temperatures and pressures necessary for sustaining partial melt post-eruption are unlikely to prevail very close to the surface (depths 0–5 km below surface), and so other explanations have been proposed: for example, steam condensates that manifest at shallow depths off the main volcanic edifice, where temperatures are reduced (Aster & Meyer, 1988; Vanorio et al., 2005; Chiarabba & Moretti, 2006; Wilks et al., 2020). These condensates may form brines that migrate towards the surface along fracture networks, explaining extensive fumarolic activity at the surface (Hudson et al., 2022; MacQueen et al., 2021). Alternatively, high V_P/V_S anomalies have been attributed to the penetration of meteoric water into the volcanic cone through fractures (Bushenkova et al., 2019; Koulakov et al., 2021).

The shallowest part of our model shows high V_P/V_S anomalies (> 1.9) to the north and south of the caldera that coincide with low V_P and low V_S anomalies. These anomalies are in the very shallow subsurface, meaning that they are constrained by only one seismic station. Therefore, in the absence of further geophysical constraints, such as magneto-telluric surveys, fluid sampling and analysis or well-log data, it is possible that these anomalies are artefacts.

5.4 The Crustal Substructure Beneath Nabro Caldera

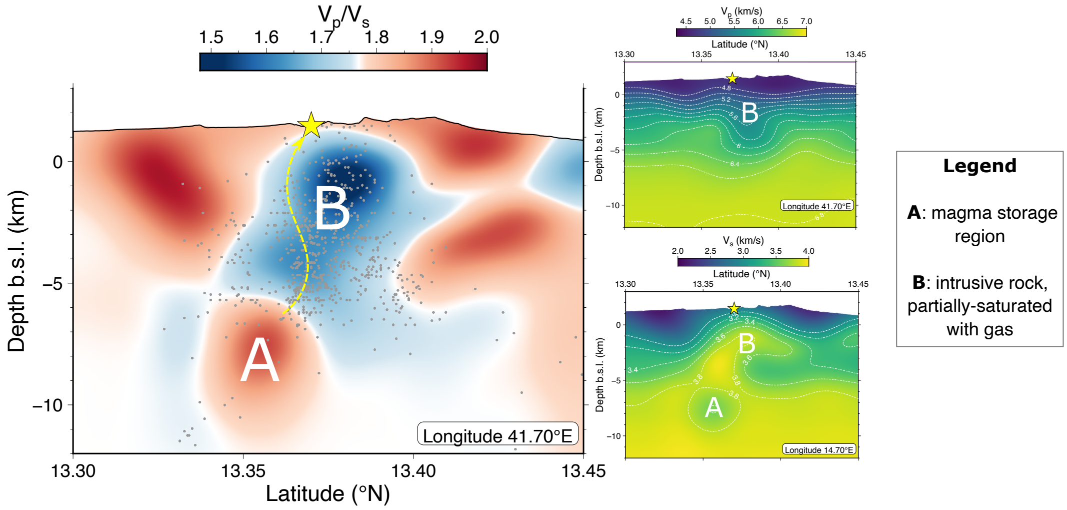

Figure 7. The V_P/V_S (left image), V_P (top right image) and V_S (bottom right image) solution models plotted along the 41.7°E cross-section beneath Nabro. To aid visualisation, contours are added to the V_P and V_S models for velocities greater than 4.8 km/s and 3.0 km/s respectively. A) The aseismic high V_P/V_S, low V_P and low V_S magma storage region is described in Section 5.3.1. B) The very low V_P/V_S and high V_S region is described in Section 5.3.2; we interpret this as a zone of intrusive rock, potentially in a stacked sill structure. The region hosts fractured, partially-saturated rocks with low V_P values. The yellow star marks the vent location of the 2011 eruption. Earthquakes located within ±1 km of the cross-section are plotted as grey circles. The yellow dashed arrow indicates a potential degassing pathway from the region of partial melt to the surface, following the densest clusters of seismicity.

Nabro is an active volcano that experienced subsidence and seismicity following its 2011 eruption. Figure 7 provides an overview of the results and interpretations of the seismic anomalies identified in this study, as summarized below.

An aseismic region of low V_P, low V_S and high V_P/V_S ratio at depths of 6–10 km (region A in Figure 7) likely represents a storage region of partially molten material, and is consistent with the results of previous geodetic, petrological and seismic studies. It is likely that partial melt has remained stored here post-eruption, as only a small fraction of the total volume of melt stored in a reservoir is generally erupted at the surface (Greenfield & White, 2015; White et al., 2019). The cause of surface subsidence is likely degassing of volatiles from this magma storage region (Hamlyn et al., 2014; Donovan et al., 2018).

Above the zone of partial melt, we observe a region of abundant seismicity and high V_S (region B in Figure 7), which we interpret as a zone of intrusive rocks from previous eruptions. These could exist in a stacked sill structure, the fine details of which we are unable to resolve with our tomographic model. This region contains the conduit that fed the 2011 eruption, which is formed of fractured, cracked rocks partially-saturated with over-pressurized gases (a mixture of CO_2 and H_2O), leading to low V_P and very low V_P/V_S ratio. The magma storage region below is a likely cause of the overpressure in these gases.

The influence of this shallow heat source on the outflow of gases through the subsurface means that Nabro is likely to have geothermal potential that may be exploited as an energy resource.

Previous studies are in agreement with our interpretations of the velocity structure at Nabro. By inverting the deformation field from satellite InSAR images, Hamlyn et al. (2018) explain the subsidence as the deflation of a Mogi source located at 6.4 ± 0.3 km depth b.s.l.. This coincides with Donovan et al. (2018)'s findings that most melt inclusions in erupted lava were trapped at 5–10 km depth b.s.l.. Their petrological study of erupted products from the 2011 eruption concludes that distinct batches of magma were stored in sills and mixed together prior to eruption (Donovan et al., 2018). A study of the post-eruption seismicity also identifies an aseismic magma storage zone at depths of 6–9 km b.s.l. (Lapins, 2021a). Numerous fumaroles have been observed at Nabro after the eruption, which has led to its identification as a region of geothermal interest (Yohannes, 2012).

5.5 Comparisons with Other Volcanoes

As an off-rift caldera in the under-studied East African Rift System that erupted months prior to the seismic deployment, there are no previous seismic tomography studies that allow for direct comparison to Nabro. However, it is still instructive to examine a few examples of volcanoes that share certain similar features with it.

Koryaksky volcano in Kamchatka erupted months before the seismic events used in the tomographic study of Bushenkova et al. (2019) were recorded. Despite the different tectonic setting, the tomographic images show a similar structure to Nabro. At depth, a high V_P/V_S anomaly represents a magma storage region. Above this, there is a low V_P/V_S anomaly associated with a vertical seismicity cluster, marking the pathway of fluid ascent. Another actively erupting volcano, Kīlauea in Hawaii, shows elevated V_P and V_S at depth, interpreted as representing the high-velocity cumulates of the volcanic core (Lin et al., 2014). An anomalous body of low V_P, low V_S and high V_P/V_S at 8–11 km depth is explained as a crustal magma reservoir. Both of these features are also observed at Nabro. The Kīlauea images also show a region of low V_P/V_S above the magma reservoir, but this is not interpreted.

Aluto volcano is also located in the East African Rift System, situated in the Main Ethiopian Rift. The seismic tomography study of Wilks et al. (2020) finds a large low velocity, high V_P/V_S zone at depths of 4–9 km, interpreted as a more ductile and melt-bearing region. Away from the volcano, there are shallow, localized high V_P/V_S regions, representing steam condensates which may form brines that migrate to the surface. A hydrothermal system with very low V_P/V_S is observed at shallow depths, hosting gases exsolved from the deeper melt body. These features are broadly similar to what is seen beneath Nabro. The main difference is that Nabro's low V_P/V_S region extends to greater depths. Despite a recent increase in surface deformation, Aluto has been quiescent for thousands of years. Therefore, the crustal substructure of Aluto could represent a 'steady-state' situation for volcanoes in the region, from which Nabro has been disturbed due to its recent eruption and the ascent of magmatic fluid from depth.

5.6 Limitations and Future Work

A fundamental limitation on our results is the resolution of the tomographic inversion, likely caused by the small size of the seismic network deployed at Nabro. Jointly inverting for velocity structure and event relocation with such a small seismic array is challenging. This is reflected in the large relocation offsets observed in particular for events outside of the aperture of the seismic network, which subsequently are removed from the catalog. Indeed, checkerboard sensitivity tests demonstrate that outside of the seismic array and deeper than ~10 km b.s.l., we cannot recover synthetic velocity perturbations. Recovery of velocity anomalies on scales of < 2 km is also limited. Therefore, we restrict our interpretations of the tomographic images to velocity anomalies occurring on scales > 4 km, within the seismic network and in the uppermost 10 km of the crust.

We are also limited in our interpretations by the lack of other observations at Nabro. Studies such as magneto-telluric surveys, geochemical analyses of volcanic fluids and well-log data would all help to provide further constraints on the interpretations presented here. The resolution of seismic velocity structure is poor at depths greater than 10 km b.s.l., due to the distribution of seismicity being mostly located at shallower depths. Thus it is difficult to form broader conclusions about magmatic processes in the mid-lower crust.

Future work could involve attempts to probe the lower crust at Nabro, e.g., through receiver function analysis (e.g., Janiszewski et al., 2020; Hammond, 2014) or an investigation of seismic anisotropy using shear-wave splitting (e.g., Nowacki et al., 2018), in order to understand how off-rift magmatism at Nabro is sustained and supplied. The application of U-GPD to seismic datasets from other volcanoes, particularly those in a post-eruptive state, would also provide useful points of comparison to this study.

6 Conclusion

We use a seismic catalog created by a deep learning model for automating phase arrival detection to invert for the earthquake locations and the 3D velocity structure beneath Nabro caldera, an off-rift volcano in the Afar region. This has produced the first tomographic images of the volcano, which was unmonitored before its explosive eruption in June 2011.

The main findings of the tomographic study are: 1) an aseismic region of low V_P, low V_S and high V_P/V_S at depths of 6–10 km b.s.l., interpreted as the primary melt storage region that fed the 2011 eruption; 2) a region of high seismicity, very low V_P/V_S ratio and low V_P, representing a zone of partially-saturated rocks containing gases that are over-pressurized due to degassing from the magma storage zone directly below; 3) general high V_P and V_S beneath the volcanic edifice, pointing to the existence of high-strength, solidified intrusive magmatic rocks.

Our results have demonstrated that deep learning models are an efficient way to obtain earthquake catalogs for the purposes of seismic tomography at volcanoes. Although our model cannot elucidate the origins of magma supply to Nabro at depths exceeding 10 km b.s.l., it does illustrate that this off-rift volcano has a similar shallow magmatic plumbing system to other hydrothermally active, restless volcanoes. The observations are consistent with the existence of a melt storage region at 6–10 km b.s.l. beneath Nabro. We have also uncovered a region that is high in volatile content, coupled to the degassing magmatic system, indicating that Nabro should be considered a region of geothermal interest. Our study highlights the need for further geophysical studies at Nabro.

Open Research Section

The raw seismic data used in this study are from the Nabro Urgency Array (Hammond et al., 2012), publicly available through IRIS Data Services (http://service.iris.edu/fdsnws/dataselect/1/). Full code to reproduce the U-GPD transfer learning model, perform model training, run the U-GPD model over continuous sections of data and use model picks to locate events in NonLinLoc (Lomax et al., 2000) are available at https://github.com/sachalapins/U-GPD, with the release (v1.0.0) associated with this study archived and available through Zenodo (Lapins, 2021b). The arrival time picks for the initial event catalog produced by the U-GPD model, as well as the station metadata, are also archived in a Zenodo repository (Lapins, 2022). The FMTOMO package is freely available to download at http://rses.anu.edu.au/~nick/fmt

(Rawlinson & Sambridge, 2004a). Files containing the final V_P, V_S and V_P/V_S models, and the relocated event catalog are available through Zenodo (Gauntlett et al., 2023).

Figures and maps were plotted using Generic Mapping Tools (GMT) version 6 (Wessel et al., 2019) licensed under LGPL version 3 or later, available at https://www.genericmapping-tools.org.

Acknowledgments

The authors thank Michael Bostock and Greg Waite for their helpful editorial comments. We are also grateful for the comments from Ivan Koulakov and an anonymous reviewer, which helped improve this paper. The seismic data were collected with funding from the Natural Environment Research Council (NERC) project NE/J012297/1 ("Mechanisms and implications of the 2011 eruption of Nabro volcano, Eritrea"). The UK seismic instruments and data management facilities were provided under loan number 976 by SEIS-UK at the University of Leicester. The facilities of SEIS-UK are supported by NERC under Agreement R8/H10/64. Author MG was supported by a Doctoral Training Partnership studentship from NERC [NE/S007474/1]. Author SL was supported by a GW4+ Doctoral Training Partnership studentship from the Natural Environment Research Council (NERC) [NE/L002434/1]. Author BG was funded by the Engineering and Physical Sciences Research Council (EPSRC) and the School of Earth Sciences at the University of Bristol. We gratefully acknowledge the cooperation we received from the Eritrea Institute of Technology, Eritrean government, Southern and Northern Red Sea Administrations, local sub-zones and village administrations. We thank the Department of Mines, Ministry of Energy and Mines for their continued support throughout the project. Special thanks go to Zerai Berhe, Mebrahtu Fisseha, Michael Eyob, Ahmed Mohammed, Kibrom Nerayo, Asresehey Ogbatsien, Andemichael Solomon and Isaac Tuum. We thank Alem Kibreab for vital help in facilitating the fieldwork. We would also like to acknowledge helpful comments from Tarje Nissen-Meyer and Lara Wagner on the initial results of this study. The tomographic inversions were carried out using the University of Oxford Advanced Research Computing service; we thank Andrew Walker for his assistance with this. IRIS Data Services are funded through the Seismological Facilities for the Advancement of Geoscience (SAGE) Award of the National Science Foundation under Cooperative Support Agreement EAR-1851048.

References

Afanasyev, A., Blundy, J., Melnik, O., & Sparks, S. (2018). Formation of magmatic brine lenses via focussed fluid-flow beneath volcanoes. *Earth and Planetary Science Letters*, *486*, 119–128.

Aloisi, M., Cocina, O., Neri, G., Orecchio, B., & Privitera, E. (2002). Seismic tomography of the crust underneath the Etna volcano, Sicily. *Physics of the Earth and Planetary Interiors*, *134*(3-4), 139–155.

Amalokwu, K., Best, A. I., Sothcott, J., Chapman, M., Minshull, T., & Li, X.-Y. (2014). Water saturation effects on elastic wave attenuation in porous rocks with aligned fractures. *Geophysical Journal International*, *197*(2), 943–947.

Aster, R., & Meyer, R. (1988). Three-dimensional velocity structure and hypocenter distribution in the Campi Flegrei caldera, Italy. *Tectonophysics*, *149*(3-4), 195–218.

Bakker, R. R., Fazio, M., Benson, P. M., Hess, K.-U., & Dingwell, D. B. (2016). The propagation and seismicity of dyke injection, new experimental evidence. *Geophysical Research Letters*, *43*(5), 1876–1883.

Barberi, F., Bonatti, E., Marinelli, G., & Varet, J. (1974). Transverse tectonics during the split of a continent: data from the Afar rift. *Tectonophysics*, *23*(1-2), 17–29.

Blundy, J., Afanasyev, A., Tattitch, B., Sparks, S., Melnik, O., Utkin, I., & Rust,

A. (2021). The economic potential of metalliferous sub-volcanic brines. *Royal Society Open Science*, *8*(6), 202192.

Bowers, G. L. (2002). Detecting high overpressure. *The leading edge*, *21*(2), 174–177.

Brikke, N. E. A. (2010). 3D seismic traveltime tomography of the central South Island, New Zealand.

Brown, R., Kavanagh, J., Sparks, R., Tait, M., & Field, M. (2007). Mechanically disrupted and chemically weakened zones in segmented dike systems cause vent localization: Evidence from kimberlite volcanic systems. *Geology*, *35*(9), 815–818.

Bushenkova, N., Koulakov, I., Senyukov, S., Gordeev, E. I., Huang, H.-H., El Khrepy, S., & Al Arifi, N. (2019). Tomographic images of magma chambers beneath the Avacha and Koryaksky volcanoes in Kamchatka. *Journal of Geophysical Research: Solid Earth*, *124*(9), 9694–9713.

Chiarabba, C., & Moretti, M. (2006). An insight into the unrest phenomena at the Campi Flegrei caldera from Vp and Vp/Vs tomography. *Terra Nova*, *18*(6), 373–379.

Chouet, B. A., & Matoza, R. S. (2013). A multi-decadal view of seismic methods for detecting precursors of magma movement and eruption. *Journal of Volcanology and Geothermal Research*, *252*, 108–175.

Christensen, N. I. (1996). Poisson's ratio and crustal seismology. *Journal of Geophysical Research: Solid Earth*, *101*(B2), 3139–3156.

Dawson, P., Chouet, B., & Pitt, A. (2016). Tomographic image of a seismically active volcano: Mammoth Mountain, California. *Journal of Geophysical Research: Solid Earth*, *121*(1), 114–133.

de Kool, M., Rawlinson, N., & Sambridge, M. (2006). A practical grid-based method for tracking multiple refraction and reflection phases in three-dimensional heterogeneous media. *Geophysical Journal International*, *167*(1), 253–270.

Donovan, A., Blundy, J., Oppenheimer, C., & Buisman, I. (2018). The 2011 eruption of Nabro volcano, Eritrea: perspectives on magmatic processes from melt inclusions. *Contributions to Mineralogy and Petrology*, *173*(1), 1–23.

Eberhart-Phillips, D., & Reyners, M. (2012). Imaging the Hikurangi Plate interface region, with improved local-earthquake tomography. *Geophysical Journal International*, *190*(2), 1221–1242.

Evans, J. R., Eberhart-Phillips, D., & Thurber, C. (1994). *User's manual for SIMULPS12 for imaging Vp and Vp/Vs; a derivative of the" thurber" tomographic inversion simul3 for local earthquakes and explosions* (Tech. Rep.). US Geological Survey,.

Foulger, G. R., Julian, B., Pitt, A., Hill, D., Malin, P., & Shalev, E. (2003). Three-dimensional crustal structure of Long Valley caldera, California, and evidence for the migration of CO2 under Mammoth Mountain. *Journal of Geophysical Research: Solid Earth*, *108*(B3).

Fromm, M., Kablick III, G., Nedoluha, G., Carboni, E., Grainger, R., Campbell, J., & Lewis, J. (2014). Correcting the record of volcanic stratospheric aerosol impact: Nabro and Sarychev Peak. *Journal of Geophysical Research: Atmospheres*, *119*(17), 10–343.

Gauntlett, M., Hudson, T., Kendall, J.-M., Rawlinson, N., Blundy, J., Lapins, S., ... Ogubazghi, G. (2023, April). *Nabro 3D velocity model produced by the FMTOMO code.* Zenodo. Retrieved from `https://doi.org/10.5281/zenodo.7701958` doi: 10.5281/zenodo.7701958

Ginzburg, A., Makris, J., Fuchs, K., & Prodehl, C. (1981). The structure of the crust and upper mantle in the Dead Sea rift. *Tectonophysics*, *80*(1-4), 109–119.

Glahn, A., Granet, M., & Group, R. G. T. (1993). Southern Rhine Graben: small-wavelength tomographic study and implications for the dynamic evolution of the graben. *Geophysical Journal International*, *113*(2), 399–418.

Goitom, B. (2017). *The Nabro volcano, tectonic framework and seismic hazard assessment of Eritrea* (Unpublished doctoral dissertation). University of Bristol.

Goitom, B., Oppenheimer, C., Hammond, J. O., Grandin, R., Barnie, T., Donovan, A., … others (2015). First recorded eruption of Nabro volcano, Eritrea, 2011. *Bulletin of Volcanology*, *77*(10), 1–21.

Greenfield, T., & White, R. S. (2015). Building Icelandic igneous crust by repeated melt injections. *Journal of Geophysical Research: Solid Earth*, *120*(11), 7771–7788.

Greenfield, T., White, R. S., & Roecker, S. (2016). The magmatic plumbing system of the Askja central volcano, Iceland, as imaged by seismic tomography. *Journal of Geophysical Research: Solid Earth*, *121*(10), 7211–7229.

Hamlyn, J., Keir, D., Wright, T. J., Neuberg, J. W., Goitom, B., Hammond, J. O., … Grandin, R. (2014). Seismicity and subsidence following the 2011 Nabro eruption, Eritrea: Insights into the plumbing system of an off-rift volcano. *Journal of Geophysical Research: Solid Earth*, *119*(11), 8267–8282.

Hamlyn, J., Wright, T., Walters, R., Pagli, C., Sansosti, E., Casu, F., … others (2018). What causes subsidence following the 2011 eruption at Nabro (Eritrea)? *Progress in Earth and Planetary Science*, *5*(1), 1–15.

Hammond, J. (2014). Constraining melt geometries beneath the Afar Depression, Ethiopia from teleseismic receiver functions: The anisotropic H-κ stacking technique. *Geochemistry, Geophysics, Geosystems*, *15*(4), 1316–1332.

Hammond, J., Goitom, B., Kendall, J. M., & Ogubazghi, G. (2012). *Nabro Urgency Array.* International Federation of Digital Seismograph Networks. Retrieved from `https://www.fdsn.org/networks/detail/4H_2011/` doi: 10.7914/SN/4H_2011

Hammond, J., Kendall, J.-M., Stuart, G., Keir, D., Ebinger, C., Ayele, A., & Belachew, M. (2011). The nature of the crust beneath the Afar triple junction: Evidence from receiver functions. *Geochemistry, Geophysics, Geosystems*, *12*(12).

Hammond, J., Kendall, M., Stuart, G., Ebinger, C., Bastow, I. D., Keir, D., … others (2013). Mantle upwelling and initiation of rift segmentation beneath the Afar Depression. *Geology*, *41*(6), 635–638.

Hauksson, E., & Shearer, P. M. (2006). Attenuation models (q_p and q_s) in three dimensions of the southern california crust: Inferred fluid saturation at seismogenic depths. *Journal of Geophysical Research: Solid Earth*, *111*(B5).

Hearn, T. M., & Clayton, R. W. (1986). Lateral velocity variations in southern California. I. Results for the upper crust from Pg waves. *Bulletin of the Seismological Society of America*, *76*(2), 495–509.

Hottmann, C., & Johnson, R. (1965). Estimation of formation pressures from log-derived shale properties. *Journal of Petroleum Technology*, *17*(06), 717–722.

Hudson, T. S., Kendall, J.-M., Pritchard, M. E., Blundy, J. D., & Gottsmann, J. H. (2022). From slab to surface: Earthquake evidence for fluid migration at Uturuncu volcano, Bolivia. *Earth and Planetary Science Letters*, *577*, 117268.

Ito, H., DeVilbiss, J., & Nur, A. (1979). Compressional and shear waves in saturated rock during water-steam transition. *Journal of Geophysical Research: Solid Earth*, *84*(B9), 4731–4735.

Janiszewski, H. A., Wagner, L. S., & Roman, D. C. (2020). Aseismic mid-crustal magma reservoir at cleveland volcano imaged through novel receiver function analyses. *Scientific reports*, *10*(1), 1–9.

Julian, B. R., Pitt, A., & Foulger, G. (1998). Seismic image of a CO2 reservoir beneath a seismically active volcano. *Geophysical Journal International*, *133*(1), F7–F10.

Kennett, B., Sambridge, M., & Williamson, P. (1988). Subspace methods for large inverse problems with multiple parameter classes. *Geophysical Journal Interna-*

tional, *94*(2), 237–247.

Kiser, E., Palomeras, I., Levander, A., Zelt, C., Harder, S., Schmandt, B., … Ulberg, C. (2016). Magma reservoirs from the upper crust to the Moho inferred from high-resolution Vp and Vs models beneath Mount St. Helens, Washington State, USA. *Geology*, *44*(6), 411–414.

Korger, E., & Schlindwein, V. (2014). Seismicity and structure of the 85 E volcanic complex at the ultraslow spreading Gakkel Ridge from local earthquake tomography. *Geophysical Journal International*, *196*(1), 539–551.

Koulakov, I., Komzeleva, V., Smirnov, S. Z., & Bortnikova, S. B. (2021). Magma-Fluid Interactions Beneath Akutan Volcano in the Aleutian Arc Based on the Results of Local Earthquake Tomography. *Journal of Geophysical Research: Solid Earth*, *126*(3), e2020JB021192.

Lapins, S. (2021a). *Detecting and characterising seismicity associated with volcanic and magmatic processes through deep learning and the continuous wavelet transform* (Unpublished doctoral dissertation). University of Bristol, http://hdl.handle.net/1983/ea90148c-a1b2-47ae-afad-5dd0a8b5ebbd.

Lapins, S. (2021b, February). *Python notebooks to accompany paper 'A Little Data Goes a Long Way: Automating Seismic Phase Arrival Picking at Nabro Volcano with Transfer Learning'.* Zenodo. Retrieved from `https://doi.org/10.5281/zenodo.4558154` doi: 10.5281/zenodo.4558154

Lapins, S. (2022, December). *Nabro volcano event catalogue from Lapins et al., 2021, JGR Solid Earth.* Zenodo. Retrieved from `https://doi.org/10.5281/zenodo.7398824` doi: 10.5281/zenodo.7398824

Lapins, S., Goitom, B., Kendall, J.-M., Werner, M. J., Cashman, K. V., & Hammond, J. O. (2021). A little data goes a long way: Automating seismic phase arrival picking at Nabro volcano with transfer learning. *Journal of Geophysical Research: Solid Earth*, *126*(7), e2021JB021910.

Lees, J. M. (1992). The magma system of Mount St. Helens: non-linear high-resolution P-wave tomography. *Journal of volcanology and geothermal research*, *53*(1-4), 103–116.

Lees, J. M. (2007). Seismic tomography of magmatic systems. *Journal of Volcanology and Geothermal Research*, *167*(1-4), 37–56.

Lin, G. (2013). Seismic investigation of magmatic unrest beneath Mammoth Mountain, California, USA. *Geology*, *41*(8), 847–850.

Lin, G., Amelung, F., Lavallée, Y., & Okubo, P. G. (2014). Seismic evidence for a crustal magma reservoir beneath the upper east rift zone of Kilauea volcano, Hawaii. *Geology*, *42*(3), 187–190.

Lomax, A., Virieux, J., Volant, P., & Berge-Thierry, C. (2000). Probabilistic earthquake location in 3D and layered models. In *Advances in seismic event location* (pp. 101–134). Springer.

Londoño, J. M., & Sudo, Y. (2003). Velocity structure and a seismic model for Nevado del Ruiz Volcano (Colombia). *Journal of Volcanology and Geothermal Research*, *119*(1-4), 61–87.

Maccaferri, F., Rivalta, E., Keir, D., & Acocella, V. (2014). Off-rift volcanism in rift zones determined by crustal unloading. *Nature Geoscience*, *7*(4), 297–300.

MacQueen, P., Gottsmann, J., Pritchard, M. E., Young, N., Ticona J, F., Ticona, E. T., & Tintaya, R. (2021). Dissecting a Zombie: Joint analysis of density and resistivity models reveals shallow structure and possible sulfide deposition at Uturuncu Volcano, Bolivia. *Frontiers in Earth Science*, 755.

Manighetti, I., Tapponnier, P., Courtillot, V., Gallet, Y., Jacques, E., & Gillot, P.-Y. (2001). Strain transfer between disconnected, propagating rifts in Afar. *Journal of Geophysical Research: Solid Earth*, *106*(B7), 13613–13665.

Molina, I., Kumagai, H., Le Pennec, J.-L., & Hall, M. (2005). Three-dimensional P-wave velocity structure of Tungurahua Volcano, Ecuador. *Journal of Volcanology and Geothermal Research*, *147*(1-2), 144–156.

Nowacki, A., Wilks, M., Kendall, J.-M., Biggs, J., & Ayele, A. (2018). Characterising hydrothermal fluid pathways beneath Aluto volcano, Main Ethiopian Rift, using shear wave splitting. *Journal of Volcanology and Geothermal Research*, *356*, 331–341.

Oppenheimer, C., Khalidi, L., Gratuze, B., Iverson, N., Lane, C., Vidal, C., ... others (2019). Risk and reward: Explosive eruptions and obsidian lithic resource at Nabro volcano (Eritrea). *Quaternary Science Reviews*, *226*, 105995.

Patane, D., Chiarabba, C., Cocina, O., De Gori, P., Moretti, M., & Boschi, E. (2002). Tomographic images and 3D earthquake locations of the seismic swarm preceding the 2001 Mt. Etna eruption: evidence for a dyke intrusion. *Geophysical Research Letters*, *29*(10), 135–1.

Paulatto, M., Minshull, T., Baptie, B., Dean, S., Hammond, J. O., Henstock, T., ... others (2010). Upper crustal structure of an active volcano from refraction/reflection tomography, Montserrat, Lesser Antilles. *Geophysical Journal International*, *180*(2), 685–696.

Pikington, P. (1988). Uses of pressure and temperature data in exploration and now developments in overpressure detection. *Journal of petroleum technology*, *40*(05), 543–549.

Pilia, S., Rawlinson, N., Direen, N., Cummins, P. R., & Balfour, N. (2013). Structural controls on localized intraplate deformation and seismicity in Southern Australia: Insights from local earthquake tomography of the Flinders Ranges. *Journal of Geophysical Research: Solid Earth*, *118*(5), 2176–2190.

Pritchard, M., Mather, T., McNutt, S. R., Delgado, F., & Reath, K. (2019). Thoughts on the criteria to determine the origin of volcanic unrest as magmatic or non-magmatic. *Philosophical Transactions of the Royal Society A*, *377*(2139), 20180008.

Pürschel, M., Gloaguen, R., & Stadler, S. (2013). Geothermal activities in the Main Ethiopian Rift: hydrogeochemical characterization of geothermal waters and geothermometry applications (Dofan-Fantale, Gergede-Sodere, Aluto-Langano). *Geothermics*, *47*, 1–12.

Rawlinson, N., & Kennett, B. (2008). Teleseismic tomography of the upper mantle beneath the southern lachlan orogen, australia. *Physics of the Earth and Planetary Interiors*, *167*(1-2), 84–97.

Rawlinson, N., Reading, A. M., & Kennett, B. L. (2006). Lithospheric structure of Tasmania from a novel form of teleseismic tomography. *Journal of Geophysical Research: Solid Earth*, *111*(B2).

Rawlinson, N., & Sambridge, M. (2004a). Multiple reflection and transmission phases in complex layered media using a multistage fast marching method. *Geophysics*, *69*(5), 1338–1350.

Rawlinson, N., & Sambridge, M. (2004b). Wave front evolution in strongly heterogeneous layered media using the fast marching method. *Geophysical Journal International*, *156*(3), 631–647.

Rawlinson, N., Sambridge, M., et al. (2003). Seismic traveltime tomography of the crust and lithosphere. *Advances in geophysics*, *46*, 81–199.

Rawlinson, N., & Spakman, W. (2016). On the use of sensitivity tests in seismic tomography. *Geophysical Journal International*, *205*(2), 1221–1243.

Rawlinson, N., Tkalčić, H., & Reading, A. M. (2010). Structure of the Tasmanian lithosphere from 3D seismic tomography. *Australian Journal of Earth Sciences*, *57*(4), 381–394.

Reinsch, T., Dobson, P., Asanuma, H., Huenges, E., Poletto, F., & Sanjuan, B. (2017). Utilizing supercritical geothermal systems: a review of past ventures and ongoing research activities. *Geothermal Energy*, *5*(1), 1–25.

Ross, Z. E., Meier, M.-A., Hauksson, E., & Heaton, T. H. (2018). Generalized seismic phase detection with deep learningshort note. *Bulletin of the Seismological Society of America*, *108*(5A), 2894–2901.

Sanders, C., Ponko, S., Nixon, L., & Schwartz, E. (1995). Seismological evidence for magmatic and hydrothermal structure in Long Valley caldera from local earthquake attenuation and velocity tomography. *Journal of Geophysical Research: Solid Earth*, *100*(B5), 8311–8326.

Sethian, J. A. (1996). A fast marching level set method for monotonically advancing fronts. *Proceedings of the National Academy of Sciences*, *93*(4), 1591–1595.

Sethian, J. A., & Popovici, A. M. (1999). 3-d traveltime computation using the fast marching method. *Geophysics*, *64*(2), 516–523.

Shalev, E., Kenedi, C., Malin, P., Voight, V., Miller, V., Hidayat, D., ... others (2010). Three-dimensional seismic velocity tomography of Montserrat from the SEA-CALIPSO offshore/onshore experiment. *Geophysical Research Letters*, *37*(19).

Theys, N., Campion, R., Clarisse, L., Brenot, H., Gent, J. v., Dils, B., ... others (2013). Volcanic SO2 fluxes derived from satellite data: a survey using OMI, GOME-2, IASI and MODIS. *Atmospheric Chemistry and Physics*, *13*(12), 5945–5968.

Thurber, C. (1993). Local earthquake tomography: velocities and V_p/V_s-Theory. *Seismic tomography: theory and practice*, 563–583.

Toksöz, M. N., Cheng, C., & Timur, A. (1976). Velocities of seismic waves in porous rocks. *Geophysics*, *41*(4), 621–645.

Vanorio, T., Virieux, J., Capuano, P., & Russo, G. (2005). Three-dimensional seismic tomography from P wave and S wave microearthquake travel times and rock physics characterization of the Campi Flegrei Caldera. *Journal of Geophysical Research: Solid Earth*, *110*(B3).

Walck, M. C. (1988). Three-dimensional VP/VS variations for the Coso region, California. *Journal of Geophysical Research: Solid Earth*, *93*(B3), 2047–2052.

Wang, Z., & Nur, A. (1986). Effect of temperature on wave velocities in sands and sandstones with heavy hydrocarbons: 56th Ann. *Internat. Mtg., Soc. Expl. Geophys*.

Wessel, P., Luis, J., Uieda, L., Scharroo, R., Wobbe, F., Smith, W. H., & Tian, D. (2019). The generic mapping tools version 6. *Geochemistry, Geophysics, Geosystems*, *20*(11), 5556–5564.

White, R. S., Edmonds, M., Maclennan, J., Greenfield, T., & Agustsdottir, T. (2019). Melt movement through the Icelandic crust. *Philosophical Transactions of the Royal Society A*, *377*(2139), 20180010.

Wiart, P., & Oppenheimer, C. (2005). Large magnitude silicic volcanism in north Afar: the Nabro Volcanic Range and Ma'alalta volcano. *Bulletin of Volcanology*, *67*(2), 99–115.

Wilks, M. (2016). *A seismological investigation into tectonic, magmatic and hydrothermal processes at Aluto and Corbetti, two restless volcanoes in the Main Ethiopian Rift* (Unpublished doctoral dissertation). University of Bristol.

Wilks, M., Kendall, J.-M., Nowacki, A., Biggs, J., Wookey, J., Birhanu, Y., ... Bedada, T. (2017). Seismicity associated with magmatism, faulting and hydrothermal circulation at Aluto Volcano, Main Ethiopian Rift. *Journal of Volcanology and Geothermal Research*, *340*, 52–67.

Wilks, M., Rawlinson, N., Kendall, J.-M., Nowacki, A., Biggs, J., Ayele, A., & Wookey, J. (2020). The coupled magmatic and hydrothermal systems of the restless Aluto caldera, Ethiopia.

Winkler, K., & Nur, A. (1979). Pore fluids and seismic attenuation in rocks. *Geophysical Research Letters*, *6*(1), 1–4.

Yohannes, E. (2012). Geothermal development in Eritrea: A country update. In *Proceedings 4th african rift geothermal conference.*

Zenonos, A., De Siena, L., Widiyantoro, S., & Rawlinson, N. (2019). P and S wave travel time tomography of the SE Asia-Australia collision zone. *Physics of the Earth and Planetary Interiors*, *293*, 106267.

Zhu, W., & Beroza, G. C. (2019). PhaseNet: a deep-neural-network-based seismic arrival-time picking method. *Geophysical Journal International*, *216*(1), 261–273.